Generation Conditions of Dacite and Rhyodacite via the Crystallization of an Andesitic Magma. Implications for the Plumbing System at Santorini (Greece) and the Origin of Tholeiitic or Calc-alkaline Differentiation Trends in Arc Magmas

Joan Andújar, Bruno Scaillet, Michel Pichavant, Timothy H. Druitt

JOURNAL OF PETROLOGY

Journal of Petrology, 2016, Vol. 57, No. 10, 1887–1920
doi: 10.1093/petrology/egw061
Original Article

OXFORD

Generation Conditions of Dacite and Rhyodacite via the Crystallization of an Andesitic Magma. Implications for the Plumbing System at Santorini (Greece) and the Origin of Tholeiitic or Calc-alkaline Differentiation Trends in Arc Magmas

Joan Andújar[1,2,3]*, Bruno Scaillet[1,2,3], Michel Pichavant[1,2,3] and Timothy H. Druitt[4]

[1]Université d'Orléans, ISTO, UMR 7327, 45071 Orléans, France; [2]CNRS/INSU, ISTO, UMR 7327, 45071 Orléans, France; [3]BRGM, ISTO, UMR 7327, BP 36009, 45060 Orléans, France; [4]Laboratoire Magmas et Volcans, Université Blaise Pascal–CNRS–IRD, OPGC, 5 Rue Kessler, 63038 Clermond-Ferrand, France

*Corresponding author. Telephone: (+33) 2 38 25 54 04. Fax: (+33) 02 38 63 64 88.
E-mail: Juan.Andujar@cnrs-orleans.fr

Received July 12, 2015; Accepted September 12, 2016

ABSTRACT

Andesitic arc volcanism is the most common type of subduction-related magmatism on Earth. How these melts are generated and under which conditions they evolve towards silica-rich liquids is still a matter of discussion. We have performed crystallization experiments on a representative andesite sample from the Upper Scoriae 1 (USC-1) eruption of Santorini (Greece) with the aim of understanding such processes. Experiments were performed between 1000 and 900 °C, in the pressure range 100–400 MPa, at fO_2 from QFM (quartz–fayalite–magnetite) to NNO (nickel–nickel oxide) + 1·5, with H_2O_{melt} contents varying from saturation to nominally dry conditions. The results show that the USC-1 andesitic magma was generated at 1000 °C and 12–15 km depth (400 MPa), migrated to shallower levels (8 km; 200 MPa) and intruded into a partially crystallized dacitic magma body. The magma cooled to 975 °C and generated the phenocryst assemblage and compositional zonations that characterize the products of this eruption. An injection of basaltic magma problably subsequently triggered the eruption. In addition to providing the pre-eruptive conditions of the USC-1 magma, our experiments also shed light on the generation conditions of silica-rich magmas at Santorini. Experimental of runs performed at $fO_2 \sim$ NNO + 1 (± 0·5) closely mimic the compositional evolution of magmas at Santorini whereas those at reduced conditions (QFM) do not. Glasses from runs at 1000–975 °C encompass the magma compositions of intermediate-dominated eruptions, whereas those at 950–900 °C reproduce the silicic-dominated eruptions. Altogether, the comparison between our experimental results and natural data for major recent eruptions from Santorini shows that different magma reservoirs, located at different levels, were involved during highly energetic events. Our results suggest that fractionation in deep reservoirs may give rise to magma series with a tholeiitic signature whereas at shallow levels calc-alkaline trends are produced.

Key words: phase equilibria; andesite; liquid line of descent; experimental petrology; Santorini; tholeiitic; calc-alkaline

INTRODUCTION

The origin of arc andesites and their relationships with their silicic counterparts (dacites and rhyolites) is still a matter of debate. Various models have been discussed in the literature to explain the origin of these melts: (1) andesites are the by-products of basalt crystallization (e.g. Gill, 1981; Pichavant *et al.*, 2002; Andújar *et al.*, 2015); (2) andesites arise from mixing between rhyolite and basalt (i.e. Eichelberger, 1978; Ruprecht *et al.*, 2012); (3) andesite liquids are direct melting products of subducting oceanic crust (e.g. Green & Ringwood, 1968; Castro *et al.*, 2013). Regardless of which, if any, of the above mechanisms dominates, an important question is to understand under which conditions andesitic melts evolve towards silica-rich compositions, and in particular whether this process occurs in a single reservoir or in multiple reservoirs located at different depths. This is crucial for understanding the final storage depth of more evolved liquids and the structure of the plumbing system beneath a volcano, as the generation level of the silica-rich melts may not correspond to that of their pre-eruptive storage. We address this issue by unravelling the parent–daughter relationships between andesites and recent dacites–rhyodacites at Santorini (Greece), to understand the evolution of the plumbing system with time at this volcanic center.

Santorini is one of the largest volcanoes in the Aegean region of Greece, with an activity characterized by multiple, large, explosive eruptions, some of which caused caldera collapse, separated in time by periods of effusive edifice construction and weaker explosive activity (Druitt *et al.*, 1999). The most recent caldera-forming eruption was the 'Minoan' eruption some 3·6 kyr ago (Bond & Sparks, 1976; Heiken & McCoy, 1984; Druitt, 2014). Magmas at Santorini range from basalt to andesite, dacite and rhyodacite, with calc-alkaline to weakly tholeiitic affinities (Nichols, 1971*a*; Druitt *et al.*, 1999). Lavas and minor explosive events emitted all types of magmas, whereas the products of large explosive eruptions are restricted to andesitic, dacitic and rhyodacitic compositions (Druitt *et al.*, 1999; Vespa *et al.*, 2006). The occurrence of large explosive events ejecting voluminous amounts of crystal-poor andesitic magma is a notable feature of Santorini volcanism (Druitt *et al.*, 1989, 1999; Mellors & Sparks, 1991). Nevertheless, previous studies of magma genesis and pre-eruptive magma storage at Santorini have focused either on rhyodacitic to dacitic (Cottrell *et al.*, 1999; Druitt *et al.*, 1999; Gertisser *et al.*, 2009; Cadoux *et al.*, 2014) or basaltic (Nichols, 1971*a*; Andújar *et al.*, 2015) magmas. In comparison, the conditions that lead to the generation of large volumes of andesitic liquids, and those involving evolution from andesite to the most silica-rich compositions, are still unclear.

In this study we investigate experimentally the phase relationships of a representative andesite from Santorini, and we compare these data with natural phenocrysts and glass compositions to shed light on the pre-eruptive storage and differentiation conditions of the selected sample. We use our results to constrain the possible parent–daughter relationships between andesites and dacites–rhyodacites at Santorini. Overall, the results constrain the architecture of the plumbing system immediately prior to large andesitic explosive eruptions and thereby improve our understanding of the volcano's behaviour, which is critical for the assessment of future volcanic hazards in this area. More generally, our study also provides insight into the conditions leading to the generation of tholeiitic and calc-alkaline magmatic series in island arc environments.

GEOLOGICAL SETTING

Santorini forms part of the Hellenic volcanic arc of the Aegean Sea, which owes its origin to the subduction of the African plate beneath the Eurasian plate (Fig. 1; Le Pichon & Angelier, 1979; Papazachos *et al.*, 2000; Nocquet, 2012). The volcano lies on continental crust about 23 km thick (Tirel *et al.*, 2004; Karagianni & Papazachos, 2007); the boundary between the upper and lower crust is at about 15 km depth (Konstantinou, 2010).

The volcanic history of Santorini has been reconstructed by Druitt *et al.* (1999). Activity began at about 650 ka with the eruption of hornblende-bearing rhyolites, rhyodacites and minor andesites of calc-alkaline affinity (Nichols, 1971*a*). From 550 ka onwards, the volcano emitted magmas ranging from basalt to rhyodacite in composition, hornblende became scarce as a phenocryst phase, and the magmas became tholeiitic to transitional tholeiitic–calc-alkaline in character. Around 360 ka, the activity became highly explosive, with the alternation of plinian eruptions and interplinian periods of constructional activity involving effusive and weakly explosive events. Direct field evidence exists for at least four caldera collapse events associated with the large plinian eruptions. Following the Minoan eruption at about 3·6 ka, volcanic activity resumed within the caldera at 197 BC and continued until recent times (Fig. 1; Pyle & Elliott, 2006). The products of this historical volcanism have built up an $\sim$3 km^3 intracaldera edifice, the summit of which forms the islands of Palaea Kameni and Nea Kameni. The last eruption of the Kameni Volcano took place in 1950. A period of caldera unrest, involving uplift and increased seismicity, took place at Santorini in 2011–2012 (Parks *et al.*, 2012).

The products of the $<$360 ka large explosive eruptions range from andesitic to rhyodacitic in composition (Huijsmans *et al.*, 1988; Huijsmans & Barton, 1989; Druitt *et al.*, 1999). Large explosive eruptions of andesitic magma include the Upper Scoriae 1 (80 ka; Keller *et al.*, 2000; Vespa *et al.*, 2006) and Upper Scoriae 2 (54 $\pm$ 3 ka; Druitt *et al.*, 1999) eruptions. Large silicic eruptions include the Lower Pumice 1 (184 ka; Keller *et al.*, 2000; Gertisser *et al.*, 2009), Lower Pumice 2 (172 ka; Keller *et al.*, 2000; Gertisser *et al.*, 2009), Cape Riva (21·8 $\pm$ 0·4 ka; Fabbro *et al.*, 2013) and Minoan

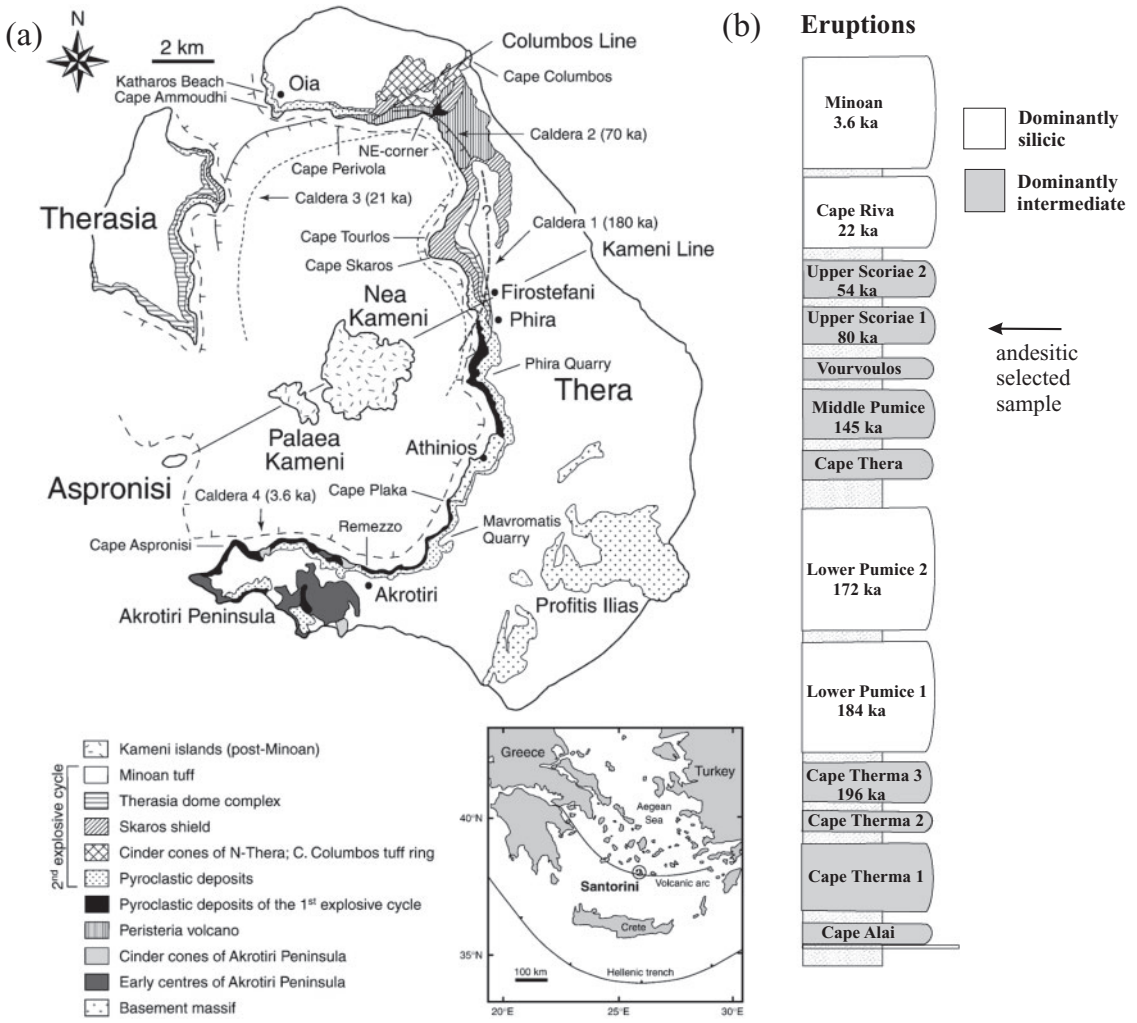

Fig. 1. (a) Simplified geological map of Santorini after Druitt *et al.* (1999). (b) Schematic stratigraphy of Santorini volcanic products, summarized from the data of Druitt *et al.* (1999). Ages are those of Druitt *et al.* (2016). The Upper Scoriae 1 eruption (80 ka) was the source for the andesitic sample used in this study. (c) Isopach map of pumice-fall deposits and vent location of the Upper Scoriae eruptions of Santorini. (d) TiO_2 (wt %) and (e) FeO* (wt %) vs SiO_2 (wt %) of Santorini magmas. The fractionation trend for Santorini magmas is shown by the grey arrow, whereas mixing models for Cape Riva and Upper Therasia andesites (grey dashed field) are shown as black lines [modified from Fabbro *et al.* (2013)]. It should be noted that the Upper Scoriae 1 (USC-1; Table 1) bulk-rock composition (star) plots on the fractionation trend, indicating that this composition is a true liquid and is genetically linked to more evolved magmas (see text for details).

(3·6 ka) eruptions (Fig. 1b). The large silicic reservoirs were dominated by rhyodacitic magma, intruded by basalt to andesite magmas immediately prior to eruption; the latter are found as mafic blebs or bands dispersed within the main silicic volume (Nichols, 1971*a*; Huijsmans *et al.*, 1988; Cottrell *et al.*, 1999; Druitt *et al.*, 1999; Gertisser *et al.*, 2009).

The Upper Scoriae 1 eruption

The Upper Scoriae 1 (USC-1) eruption started with a Plinian phase from a vent close to Nea Kameni. The first phase generated a fallout deposit up to 150 cm thick, with thin intercalated base surge layers. It subsequently generated voluminous scoria flows that were discharged mostly towards the southern parts of the island and laid down scoriaceous ignimbrite and spatter covering at least 60 km^2 (Fig. 1; Mellors & Sparks, 1991; Druitt *et al.*, 1999).

Druitt *et al.* (1999) made a cursory petrological study of the USC-1 products. They showed that the dominant (≫99%) juvenile component is an andesitic scoria with 57·7–59·1 wt % SiO_2; however, dacitic pumices with 62·0–63·2 wt % SiO_2 are present sparsely in the basal fallout layer and are interpreted as representing a small volume of more evolved magma that was co-erupted with the andesite. They reported 3–14 wt % plagioclase (Pl), clinopyroxene (Cpx), orthopyroxene (Opx) and magnetite (Mt) phenocrysts in the andesite.

With the aim of determining andesite–basalt relationships at Santorini, Andújar *et al.* (2015) performed a detailed petrographic study of the USC-1 sample that is the starting composition for the present study.

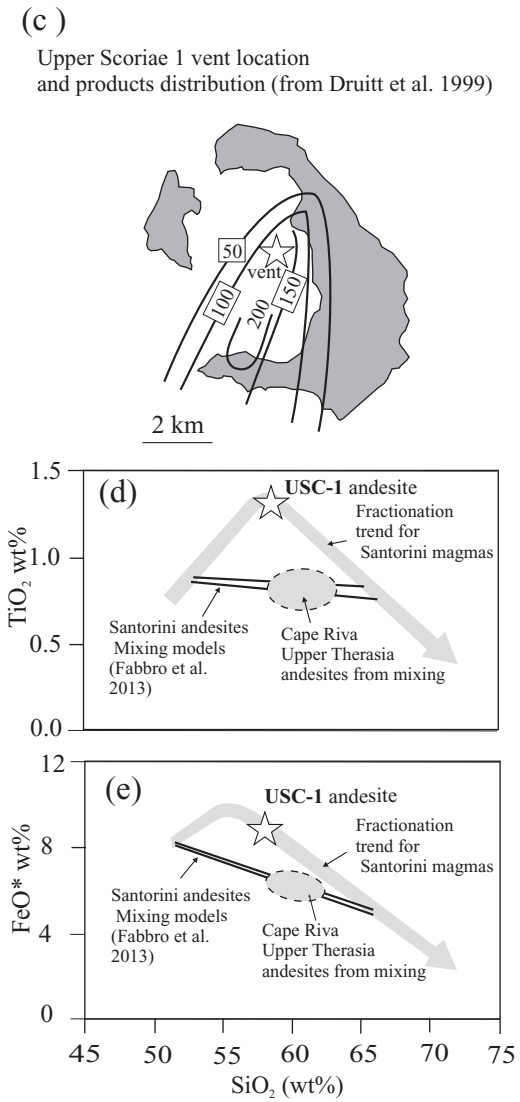

Fig. 1. Continued.

The sample is an andesitic scoria block with 28 wt % of phenocrysts set in a highly vesiculated and microcrystalline groundmass of Pl, Cpx and Mt (Table 1). The phenocrysts are euhedral to subhedral Pl (16 wt %, $An_{53\pm2.5}$), Cpx [8 wt %, either as isolated, normally zoned crystals (cores of $En_{44}Fs_{19}Wo_{37}$, Mg#70 to rims of $En_{42}Fs_{21}Wo_{37}$, Mg#67 ± 1) or as overgrowths of Mg-poorer Cpx ($En_{38}Fs_{23}Wo_{39}$, Mg#63) or pigeonite (Pig; $En_{55}Fs_{28}Wo_{16}$, Mg#67)], Mt (3 wt %), and Opx (1·3 wt %, $En_{65}Fs_{29}Wo_4$). In addition, the sample has >1·5 vol. % xenocrystic olivine (Ol) (Fo_{64}), Pig, diopside ($En_{43-45}Fs_{10-14}Wo_{43-45}$, Mg#75–81) and An-rich Pl (An_{91}). Some xenocrysts have compositional zonations suggesting partial re-equilibration with the host andesitic melt whereas others lack such features. The Mg-poor augite ($En_{38}Fs_{23}Wo_{39}$, Mg#63), low-An Pl (An_{45-50}) and resorbed Opx in the andesite have a composition similar to the phenocrysts of Santorini dacites ($En_{55}Fs_{40}Wo_4$, Mg#58; e.g. dacite from the Middle Pumice eruption; Druitt *et al.*, 1999). This and the common mantling of Cpx by an Mg-rich rim both suggest a xenocrystic origin for such Opx and Mg-poor Cpx in the andesite [see Andújar *et al.* (2015) for more details].

Phase equilibrium experiments show that Santorini basalts pond at depths of 12–14 km (400 MPa), where they fractionate to yield basaltic andesite liquids (55–58 wt % SiO_2) having up to 5 wt % dissolved H_2O (H_2O_{melt}) at around 1000 °C and at an $fO_2 \sim$ QFM (±0·3 log units), where QFM is quartz–fayalite–magnetite buffer (Andújar *et al.*, 2015). This is achieved by crystallizing about 60 wt % Ol + Cpx + Pl + Opx + Mt ± Pig ± Ilm (ilmenite). Experiments show that this phenocryst assemblage mimics physically and compositionally the mafic xenocrystic assemblage of the USC-1 andesite, indicating that the latter probably came from the mushy zone in which the andesite was produced. Altogether, the observations made by Andújar *et al.* (2015) demonstrate the complex and highly dynamic character of the plumbing system at Santorini, as already stressed by previous studies (i.e. Cottrell *et al.*, 1999; Druitt *et al.*, 1999; Michaud *et al.*, 2000; Gertisser *et al.*, 2009; Martin *et al.*, 2010).

Current thermobarometric constraints for Santorini magmas

Gardner *et al.* (1996) determined a temperature of 1000°C and H_2O_{melt} of 3 wt % for the USC-1 andesite based on analyses of glass inclusions in plagioclase phenocrysts. This temperature is in the range of homogenization temperatures of heating stage experiments (985–1005°C) performed on andesitic melt inclusions by Michaud *et al.* (2000), although those researchers reported higher water contents (5–6 wt %) estimated using the 'by difference method' (Devine *et al.*, 1995). For the more silicic products (dacite to rhyodacite), pre-eruptive constraints based on a variety of geothermometers and experimental phase equilibria were established by Cottrell *et al.* (1999) and Cadoux *et al.* (2014). Coexisting Fe–Ti oxides in dacitic to rhyodacitic products yield temperatures between 825 and 1012°C (Barton & Huijsmans, 1986; Gardner *et al.*, 1996; Cottrell *et al.*, 1999; Druitt *et al.*, 1999; Gertisser *et al.*, 2009; Cadoux *et al.*, 2014; Druitt, 2014). Water content estimates are in the range 3–4 wt % for post-caldera dacites of Nea Kameni (Barton & Huijsmans, 1986), whereas for the rhyodacitic products of the Lower Pumice 2 and Minoan eruptions, phase equilibrium experiments gave H_2O_{melt} ranging from 3 to 6 wt % (Cottrell *et al.*, 1999; Gertisser *et al.*, 2009; Cadoux *et al.*, 2014). Pressure estimates for the silicic reservoirs vary according to the researchers. Whereas Gertisser *et al.* (2009) estimated a pressure of 400 MPa for the Lower Pumice 2 reservoir by using the Al-in-hornblende geobarometer, Cottrell *et al.* (1999) and Cadoux *et al.* (2014) determined pressures up to 200 MPa for the Minoan, Lower Pumice 1, and Lower Pumice 2 units. Although Cottrell *et al.*

Table 1: Major element compositions of the bulk-rock natural Upper Scoriae 1 andesite sample from Andújar *et al.* (2015), starting material, glass and mineral phases (wt %)

	Bulk-rock	Starting material	SD	glass*	mt	SD	pl	SD	augite (Mg#67)	SD	opx	SD
n:		5			6		85		67		5	
SiO_2	58·52	59·26	0·17	62·79	0·11	0·02	55·05	1·44	49·25	0·73	52·05	0·72
TiO_2	1·30	1·30	0·02	0·98	15·14	2·29	0·07	0·13	1·01	0·12	0·33	0·06
Al_2O_3	16·04	15·60	0·17	15·82	3·02	0·56	26·61	0·74	3·54	0·66	1·09	0·51
MgO	2·84	2·47	0·06	1·78	2·64	0·50	0·08	0·11	14·20	0·44	23·49	0·77
CaO	6·55	6·44	0·25	4·82	0·07	0·06	10·40	0·54	17·46	0·81	2·09	0·19
MnO	0·19	0·22	0·06	0·19	0·50	0·22	0·04	0·05	0·42	0·12	0·63	0·10
FeO*	8·74	8·62	0·30	7·01	71·45	1·34	0·62	0·57	12·40	0·50	18·85	0·69
Na_2O	4·19	4·32	0·09	4·70	0·03	0·04	5·03	0·31	0·31	0·05	0·07	0·10
K_2O	1·40	1·54	0·02	1·90	0·02	0·03	0·20	0·11	0·02	0·02	0·02	0·03
P_2O_5	0·23	0·23	0·01									
Sum	100	100		100	93·09	1·60	98·27	1·37	92·68	1·21	98·77	1·32
Mg#					6·17	0·40			67·12	0·62	68·96	0·84
a.p.f.u.												
En									41·83		65·38	0·86
Fs									20·50		29·43	0·81
Wo									36·98		4·19	0·41
An							52·66	2·48				
Ab							46·10	2·50				
Or							1·24	0·75				
phase proportions (wt %)			3·2		15·5		7·7		1·3			

*Calculated by mass balance.
Bulk-rock analysed by inductively coupled plasma mass spectrometry; mt, magnetite; pl, plagioclase; opx, orthopyroxene; *n*, number of analysis; SD, standard deviation. FeO*, total iron reported as Fe^{2+}. En, Fs and Wo were calculated as done by Morimoto (1989). Mg# = 100Mg/(Mg + Fe*); An = 100Ca/(Ca + Na + K); Ab = 100Na/(Ca + Na + K); Or = 100K/(Ca + Na + K). End-members calculated as done by Deer *et al.* (1972).

(1999) inferred magma migration from 200 to 50 MPa before the Minoan eruption, Cadoux *et al.* (2014) concluded that all rhyodacitic magmas from the first and second explosive cycles were stored at the same pressure (~200 MPa), and that migration of magma is not necessary to explain the petrological attributes of the caldera-forming Minoan eruption. Pressure estimates obtained for the more recent dacites of Nea Kameni point to shallower depths (2–4 km, 80–150 MPa; Barton & Huijsmans, 1986). Finally, fO_2 values range between QFM – 0·5 (0·5 log unit below the quartz–fayalite–magnetite buffer; Chou, 1978) and NNO + 0·5 (0·5 log unit above the Ni–NiO buffer; Pownceby & O'Neill, 1994) for mafic to silicic compositions (Barton & Huijsmans, 1986; Cottrell *et al.*, 1999; Gertisser *et al.*, 2009; Cadoux *et al.*, 2014; Druitt, 2014; Andújar *et al.*, 2015).

Liquid line of descent and melt evolution at Santorini

Petrological and geochemical studies have already shown that the main mechanism of magma evolution at Santorini is fractional crystallization (FC; Nichols, 1971*a*; Barton *et al.*, 1983; Mann, 1983; Huijsmans *et al.*, 1988; Huijsmans & Barton, 1989; Druitt *et al.*, 1999; Michaud *et al.*, 2000; Zellmer *et al.*, 2000). This process defines a liquid line of descent (LLD) for Santorini magmas that is characterized by enrichment in FeO*, TiO_2 and P_2O_5 during the early stages; these elements reach peak values at 55–60 wt % SiO_2 (Fig. 1d and e). This trend results from the fractionation of Ol, Cpx, Pl (± Mt), which generates liquids with a tholeiitic character (Miyashiro, 1974; Druitt *et al.*, 1999). The onset of magnetite and ilmenite crystallization at ~58 wt % SiO_2 results in Fe–Ti depletion, silica enrichment and moderate alkali enrichment of the melts that characterize the more evolved magmas at Santorini (dacites, rhyodacites; Fig. 1d and e). However, the FC process alone cannot fully explain the main trends defined by the Santorini magmas. Crustal assimilation together with repeated input of mafic magma also exerts some control on magma evolution (Nichols, 1971*b*; Barton *et al.*, 1983; Huijsman *et al.*, 1988; Druitt *et al.*, 1999; Zellmer *et al.*, 2000). As a result, even if, as we argue here, the vast majority of magmas from Santorini are true fractionates, a small part of them fall off the main fractionation trend (Fig. 1d and e): such magmas are depleted in FeO* and TiO_2 and have calc-alkaline affinities compared with the FC liquids. The petrology and geochemistry of these products indicate that such magmas are hybrid products from the mixing between mafic and silicic melts (e.g. Cape Riva andesite and dacite, Upper Therasia andesite; Fabbro *et al.*, 2013).

Because we use the USC-1 andesite as the starting material for our crystallization experiments, the presence of ~1·5 wt % of xenocrystic material and its effect on phase equilibria need to be assessed. The USC-1 bulk composition (Table 1) is shown in Fig. 1d and e along with a typical fractionation trend and andesites of mixed origin. The USC-1 rock plots clearly at the TiO_2 and FeO* enrichment peak, far away from the field defined by hybrid andesites (Fig. 1d and e; Cape Riva and Therasia; Fabbro *et al.*, 2013). This observation confirms that our starting material is close to a 'true' fractionated liquid, and not a hybrid andesite.

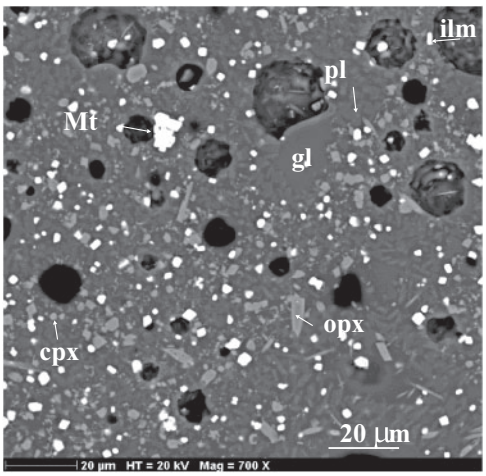

Fig. 2. Backscattered electron image of charge usc53 (950 °C, 200 MPa, $fO_2 \sim$ NNO + 1·5) containing 53 wt % of plagioclase (pl), clinopyroxene (cpx), orthopyroxene (opx), magnetite (Mt), ilmenite (ilm) and glass (gl). The high degree of crystallization, the small size of the crystals and the presence of glass pools should be noted.

EXPERIMENTAL APPROACH AND ANALYTICAL TECHNIQUES

Details concerning the starting material and capsule preparation, as well as the experimental equipment and analytical conditions used in this work, are provided in the Supplementary Data (available for downloading at http://www.petrology.oxfordjournals.org).

RESULTS

Identified phases in the run products of both oxidized (NNO + 1·5) and reduced (NNO – 0·5) experiments include glass (Gl), Cpx, Opx, Mt, Pl, Ilm, amphibole (Amph), apatite (Ap) and quartz (Qz) (Fig. 2). The experimental results are listed in Table 2 and displayed as a series of isobaric–polythermal (Fig. 3a–d) or isothermal–polybaric sections (Fig. 3e and f) showing the effects of T, P, H_2O content and fO_2 on phase relationships. The effects on melt compositions are shown in Figs 4–10. We present the experimental results depending on the prevailing fO_2 (NNO + 1·5 or QFM) and the range of temperatures 1000–975°C, 950–900°C.

Phase relationships under oxidizing conditions ($fO_2 \sim$ NNO + 1·5)

At 200 MPa and 1000 °C, Mt is the liquidus phase at water saturation (H_2O_{melt} 6·6 wt %; Table 2), and is subsequently joined by Cpx, Opx and Pl (Fig. 3a). At 975°C the stability of Pl and Opx moves towards higher water contents (6 wt %). Ilm crystallizes only at temperatures of ≤960°C and at $H_2O_{melt} \leq$ 6 wt %. Amph crystallizes at ≤930°C in the $H_2O_{melt} \geq$ 6 wt % part of the diagram (Fig. 3a), being in a broad reaction relationship with Opx, as observed in other experimental studies (e.g. Scaillet & Evans, 1999). The stability field of Qz is loosely constrained, as this phase has been identified in only one experimental charge at 200 MPa; this shows that Qz crystallization is restricted to ≤900°C and $H_2O_{melt} <$ 5 wt %.

At 400 MPa, liquidus conditions are attained at 1000°C and 9 wt % H_2O_{melt} (Fig. 3b). At this temperature, Mt and Cpx crystallize between 8 and 9 wt % H_2O_{melt}, whereast Pl and Opx appear at $H_2O_{melt} <$ 7 wt %. At temperatures <985°C, the Pl-in curve is shifted towards higher H_2O_{melt} (8–8·5 wt %), whereas Opx is not stable at $H_2O_{melt} >$ 7 wt % (Fig. 3b). The Ilm stability field has a shape similar to that observed at 200 MPa, with an upper thermal limit at ≤960°C, but is stable at higher H_2O_{melt} up to 7 wt % at 400 MPa. Amph is stable at <930°C, and in the H_2O_{melt} range 7–9 wt %. At lower H_2O_{melt} Amph breaks down to Cpx, Opx, Mt and Ilm, being involved in a similar reaction relationship to the one at 200 MPa. Qz crystallizes at 400 MPa and H_2O_{melt} < 4 wt % over the investigated temperature range (Fig. 3b; Table 2).

At 100 MPa, and for the two explored temperatures (975–1000°C), Cpx, Mt and Pl co-crystallize at water-saturated conditions (~5 wt % H_2O_{melt}), whereas Opx appears when H_2O_{melt} is slightly decreased (Fig. 3e and f).

Phase relationships at reducing conditions ($fO_2 \sim$ QFM)

A decrease in fO_2 does not affect the mineral assemblage found under more oxidizing conditions (Cpx + Opx + Plag + Mt + Ilm + Amph). Qz has not been identified, but its presence can be anticipated in the H_2O-poor part of the diagram by analogy with what is observed at NNO + 1·5. At 200 and 400 MPa, the first appearance of all phases occurs over a narrower H_2O_{melt} region compared with NNO + 1·5, in the water-rich part of the diagram (>6 to 8 wt % H_2O_{melt} depending on pressure; Fig. 3c and d); the boundary curves have steeper slopes or are almost vertical. Mt still appears at the liquidus, but Ilm stability is expanded towards higher temperatures (1000°C), whereas Opx and Pl co-crystallize at 6 wt % H_2O_{melt}. Amph is unaffected by the decrease in fO_2 from NNO + 1·5 to QFM, with an upper thermal limit at about 930°C; it appears at > 6 wt % H_2O_{melt} (Fig. 3c). At 400 MPa, the decrease in fO_2 decreases the liquidus temperatures to 980°C, and the crystallization sequence is affected in the following ways: (1) Cpx becomes the liquidus phase; (2) Ilm is shifted towards higher temperatures and water contents, appearing with Opx at 7 wt % H_2O_{melt} and 1000°C (Fig. 3d); (3) Mt and Pl are displaced toward lower H_2O_{melt} compared with NNO + 1·5 conditions, Pl being the last mineral to appear in the sequence (Fig. 3d); (4) Amph is stable at < 950°C and $H_2O_{melt} >$ 8 wt %, being again in a reaction relationship with Opx and Pl at lower water contents.

Table 2: Experimental run conditions and results

Run	XH_2O_{in}	fH_2O	H_2O_{melt}[a]	H_2O[b]	log fO_2	ΔNNO	ΔQFM	Phase assemblage											
	(mole %)	(bar)	(mole %)	(mole %)	(bar)			Mt	Ilm	Cpx	Opx	Pl	Amph	Qz	Ap	Crystal	Gl	$\sum r^2$	Pl/Opx
Oxidized experiments																			
1000°C, 200 MPa; 91 h; fH_2(bar): 2·45					−8·80	1·53													
usc62	1·00	1940	6·60	7·64	−8·76	1·53		4								4·0	96·0	0·11	
usc63	0·75	1446	5·75	7·25	−9·02	1·27		4·3		5·7						10·0	90·0	0·15	
usc64	0·52	1007	4·85		−9·33	0·96		X		X							X		
usc65	0·36	703	4·10	4·56	−9·65	0·65		5·5		8·9	1·6	24·1				40·1	59·9	0·17	15·1
usc66	0·10	194	2·24	3·60	−10·76	−0·47		X		X	X	X							
975°C, 200 MPa; 43·5 h; fH_2(bar): 2·23					−9·15	1·56													
usc32	1·00	1940	6·60	5·37	−9·10	1·58		1·7		5·4						7·1	92·9	0·12	
usc33	0·71	1378	5·62	4·47	−9·40	1·28		1·7		5·4	0·58	4·8				12·5	87·5	0·03	8·3
usc34	0·58	1123	5·11	3·69	−9·58	1·10		3·3		8·2	1·4	16·7				29·6	70·4	0·03	11·9
usc35	0·31	592	3·78	2·31	−10·13	0·55		X		X	X	X					X		
usc36	0·10	194	2·24	2·31	−11·10	−0·42		X		X	X	X					X		
950°C, 200 MPa; 75·5 h; fH_2(bar): 3·22					−9·91	1·20													
usc52	1·00	1940	6·60	6·60	−9·85	1·22		6·5		10·6	1·5	34·4				53·0	47·0	0·18	22·9
usc53	0·72	1391	5·65	4·45	−10·14	0·93		6·3	0·15	12·3	1·9	32				52·7	47·4	0·11	16·8
usc54	0·50	976	4·78	2·03	−10·45	0·62		6	0·62	14·8	1·9	44·6				67·9	32·1	0·37	23·5
usc55	0·30	588	3·77		−10·89	0·18		X	X	X	X	X					X		
usc56	0·10	194	2·24		−11·85	−0·78		X	X	X	X	X					X		
925°C, 200 MPa; 51 h; fH_2(bar): 3·03					−10·39	1·13													
usc42	1·00	1902	6·54	5·23	−10·27	1·22		5·8		6·4		11·02	5·5		trace	28·7	71·3	0·09	
usc43	0·67	1283	5·44	3·78	−10·61	0·88		6	0·4	11·9	0·91	39·6				58·8	41·2	0·17	43·5
usc44	0·47	901	4·61		−10·92	0·57		X	X	X	X	X					X		
usc45	0·30	564	3·70		−11·32	0·17		X	X	X	X	X					X		
usc46	0·10	190	2·22		−12·27	−0·78		X	X	X	X	X					X		
900°C, 200 MPa; 115 h; fH_2(bar): 2·15					−10·49	1·20													
usc57	1·00	1902	6·54		−10·44	1·49		X		X		X	X						
usc58	0·84	1596	6·02		−10·59	1·34		X		X		X	X						
usc59	0·69	1321	5·51		−10·75	1·17		X	X	X	X	X					X		
usc60	0·62	1174	5·22		−10·86	1·07		X	X	X	X	X					X		
usc61	0·52	989	4·81		−11·01	0·92		X	X	X	X	X		X			X		
1000°C, 400 MPa; 88 h; fH_2(bar): 7·40					−9·08	1·24													
usc67	1·00	4116	9·39	10·26	−9·07	1·18										0·0	100·0		
usc68	0·70	2875	7·94	5·09	−9·38	0·87		0·1		2·7						2·8	97·2	0·28	
usc69	0·53	2198	7·00	5·46	−9·62	0·64		0·6		2·7						3·3	96·7	0·09	
usc70	0·29	1196	5·26	5·41	−10·15	0·11		2		8·8	2·1	19·7				32·6	67·4	0·09	9·4
usc71	0·10	412	3·19	3·77	−11·07	−0·82		1·9		13·2	3·3	33·5				51·9	48·1	0·17	10·2
975°C, 400 MPa; 43·5 h; fH_2(bar): 4·42					−9·06	1·65													
usc37	1·00	4051	9·32	8·55	−9·06	1·58		1·3								1·3	98·7	0·5	
usc38	0·70	2833	7·88	4·69	−9·37	1·27		1·8		9·3						11·1	88·9	0·08	
usc39	0·49	1983	6·67	4·26	−9·68	0·96		3		10·4	3·1	10·7				27·2	72·8	0·15	3·5
usc40	0·29	1177	5·22	3·92	−10·13	0·51		5		8·4	5	39·2				57·6	42·4	0·1	7·8
usc41	0·10	405	3·17		−11·06	−0·42		X		X	X	X		X			X		
950°C, 400 MPa; 94 h; fH_2(bar): 5·96					−9·77	1·34													
usc77	1·00	3959	9·22	8·14	−9·77	1·27		5·4		5·7						11·1	88·9	0·25	
usc78	0·47	1880	6·50	2·99	−10·42	0·62		5·7	0·81	13·3	2·4	39·1				61·3	38·7	0·13	16·3
usc79	0·48	1915	6·56		−10·40	0·64		X	X	X	X	X					X		

(continued)

Table 2. Continued

Run	XH_2O_{in}	fH_2O	H_2O_{melt}[a]	H_2O[b]	log fO_2	ΔNNO	ΔQFM	Phase assemblage											
	(mole %)	(bar)	(mole %)	(mole %)	(bar)			Mt	Ilm	Cpx	Opx	Pl	Amph	Qz	Ap	Crystal	Gl	$\sum r^2$	Pl/Opx
usc80	0·29	1166	5·20		−10·83	0·21		X	X	X	X	X					X		
usc81	0·10	396	3·13		−11·77	−0·73		X	X	X	X	X		X			X		
925° C, 400 MPa; 50 h; fH_2(bar): 7·33					−10·39	1·13													
usc82	1·00	3849	9·10	8·28	−10·42	1·03		4·7		0·8			13·6			19·1	80·9	0·23	
usc83	0·83	3199	8·34	6·11	−10·58	0·87		3·3		3·8		10·4	15·4			32·9	67·1	0·04	
usc84	0·68	2626	7·61	5·97	−10·76	0·70		5·2		4·5		22·6	14			46·3	53·7	0·04	
usc85	0·54	2067	6·80	5·74	−10·96	0·49		5·3	1·1	12·6	6·3	45·8				71·1	28·9	0·33	7·3
usc86	0·35	1329	5·53		−11·35	0·10		X	X	X	X	X							
1000° C, 100 MPa; 43 h; fH_2(bar): 0·75					−8·37	1·96													
usc72	1·00	898	4·60	4·06	−8·41	1·91		5·1		5·2		6·7				17·0	83·0	0·33	
usc73	0·73	656	3·97	3·75	−8·68	1·63		5·5		7	1·8	15·8				30·1	69·9	0·08	8·8
usc74	0·52	467	3·38	2·17	−8·97	1·34		6·9		8·6	2·5	32·9				50·9	49·1	0·3	13·2
usc75	0·42	375	3·06	2·17	−9·16	1·15		6·5		11·8	1·6	48·1				68·0	32·0	0·18	30·1
usc76	0·10	90	1·56		−10·41	−0·09													
975° C, 100 MPa; 64·5 h; fH_2(bar): 0·72					−8·75	1·96													
usc57b	1·00	898	4·60	6·71	−8·79	1·91		5·6		6·5		8·11				20·2	79·8	0·13	
usc58b	0·70	625	3·88		−9·10	1·59		X		X	X	X					X		
usc59b	0·41	371	3·04	4·24	−9·56	1·14		X		X	X	X					X		
usc60b	0·27	239	2·47		−9·94	0·76		X		X	X	X					X		
usc61b	0·10	90	1·56		−10·79	−0·09													
Reduced experiments																			
1000° C, 200 MPa; 48 h; fH_2(bar): 13·14					−10·22	−0·07	0·62												
usc27	1·00	1940	6·60	7·48	−10·22	0·07	0·62	0·9								0·9	99·1	0·28	
usc28	0·70	1363	5·59	5·38	−10·53	−0·24	0·32	1·8	0·68	7·4	2·2	11				23·1	76·9	0·08	
usc29	0·51	984	4·80	5·08	−10·81	−0·52	0·03	X	X	X	X	X					X		
usc30	0·31	610	3·84	4·10	−11·23	−0·94	−0·38	X	X	X	X	X					X		
usc31	0·10	194	2·24		−12·22	−1·93	−1·38	X	X	X	X	X					X		
975° C, 200 MPa; 52·5 h; fH_2(bar): 53·60					−11·91	1·29	−0·69												
usc1	1·00	1940	6·60	6·65	−11·86	−1·19	−0·64	0·2		0·8						1·0	99·0	0·02	
usc16	0·91	1758	6·30		−11·95	−1·27	−0·72	X	trace	X									
usc17	0·82	1583	6·00		−12·04	−1·36	−0·81	X	trace	X	X	X							
usc2	0·68	1325	5·52	3·42	−12·19	−1·52	−0·97	2·2	0·14	7·7	3·23	17·6				30·9	69·1	0·02	
usc3	0·51	984	4·80	3·08	−12·45	−1·78	−1·23	2·1	0·12	6·3	4·2	20·8				33·5	66·5	0·08	
usc4	0·33	639	3·92	1·71	−12·83	−2·15	−1·60	X	X	X	X	X					X		
usc5	0·10	194	2·24	1·49	−13·86	−3·19	−2·64	X	X	X	X	X					X		
925° C, 200 MPa; 49 h; fH_2(bar): 10·58					−11·41	0·04	0·62												
usc6	1·00	1902	6·54		−11·35	0·14	0·67	1·8		1·2			12·4			15·4	84·6	0·52	
usc21b	0·93	1768	6·32		−11·42	0·07	0·61	X	X	X			X						
usc22b	0·81	1546	5·93		−11·53	−0·04	0·49	X	X	X	X	X							
usc7	0·72	1373	5·61		−11·64	−0·15	0·39	X	X	X	X	X					X		
usc8	0·48	915	4·64		−11·99	−0·50	0·04	X	X	X	X	X					X		
usc9	0·36	681	4·04		−12·25	−0·76	−0·22	X	X	X	X	X					X		
usc10	0·10	190	2·22		−13·35	−1·86	−1·33	X	X	X	X	X					X		
1000° C, 400 MPa; 68 h; fH_2(bar): 33·32					−10·39	−0·16	0·46												
usc22	1·00	4116	9·39	7·20	−10·38	−0·12	0·47									0·0	100·0		
usc23	0·70	2894	7·96	4·31	−10·68	−0·43	0·16			X							X		
usc24	0·53	2173	6·96		−10·93	−0·68	−0·09			X							X		

(continued)

Table 2. Continued

Run	XH_2O_{in}	fH_2O	H_2O_{melt}[a]	H_2O[b]	log fO_2	ΔNNO	ΔQFM	Phase assemblage											
	(mole %)	(bar)	(mole %)	(mole %)	(bar)			Mt	Ilm	Cpx	Opx	Pl	Amph	Qz	Ap	Crystal	Gl	$\sum r^2$	Pl/Opx
usc25	0·29	1180	5·23	2·40	−11·46	−1·21	−0·62	2·2	0·19	7·4	0·88	11·4				22·1	77·9	0·02	
usc26	0·10	412	3·19	2·10	−12·38	−2·12	−1·53	X	X	X	X	X					X		
975° C, 400 MPa; 45·85 h; fH_2(bar): 38·22					−10·94	−0·32	0·29												
usc11	1·00	4051	9·32	8·49	−10·93	−0·29	0·29									0·0	100·0		
usc18	0·93	3765	9·01		−10·99	−0·35	0·23	trace									X		
usc19	0·82	3322	8·49		−11·10	−0·46	0·12	X	X	X	X						X		
usc12	0·71	2871	7·93	6·13	−11·23	−0·59	0·00	2·1	0·1	7·9	1·5	13·5				25·1	74·9	0·11	
usc13	0·59	2393	7·28	5·39	−11·39	−0·75	−0·16	2·8	0·14	9	1·2	23·7				36·8	63·2	0·13	
usc14	0·29	1194	5·26		−11·99	−1·35	−0·77	X	X	X	X	X					X		
usc15	0·10	405	3·17		−12·93	−2·29	−1·71	X	X	X	X	X					X		
925° C, 400 MPa; 54·4 h; fH_2(bar): 59·96					−12·22	−0·77	−0·20												
usc87	1·00	3849	9·10	9·41	−12·25	−0·80	−0·22	2·8	0·18	2·8			8·46			14·2	85·8	0·16	
usc88	0·85	3268	8·43	7·22	−12·39	−0·94	−0·36	3·2	0·78	5·8			10·25			20·0	80·0	0·19	
usc89	0·72	2769	7·80	6·00	−12·54	−1·08	−0·51	4	0·24	10·5	5·3	30·1				50·1	49·9	0·1	
usc90	0·54	2092	6·84	5·95	−12·78	−1·33	−0·75	X	X	X	X	X							

XH_2O_{in}, initial $H_2O/(H_2O + CO_2)$ in the charge (in moles). H_2O_{melt}, water content in the melt:
[a]determined by the solubility model of Papale et al. (2006) and using the method of Scaillet & Macdonald (2006);
[b]determined by difference method (see text for details). fH_2, hydrogen fugacity of the experiment determined by using NiPd or CoPd alloy sensors. log fO_2, logarithm of the oxygen fugacity calculated from the experimental fH_2. ΔNNO – ΔQFM is log fO_2 – log fO_2 of the NNO or QFM buffer calculated at P and T (NNO, Pownceby & O'Neill, 1994; QFM, Chou, 1978). Crystal, numbers indicate the phase abundance in the charge in weight per cent. Mt, magnetite; Ilm, ilmenite; Cpx, clinopyroxene; Opx, orthopyroxene; Pl, plagioclase; Amph, amphibole; Qz, quartz; Ap, apatite; Gl, glass; Pl/Opx, plagioclase (wt %)/orthopyroxene (wt %) in the charge. Trace, phase with a modal abundance <0·1 wt %. X, mineral phase identified with SEM.

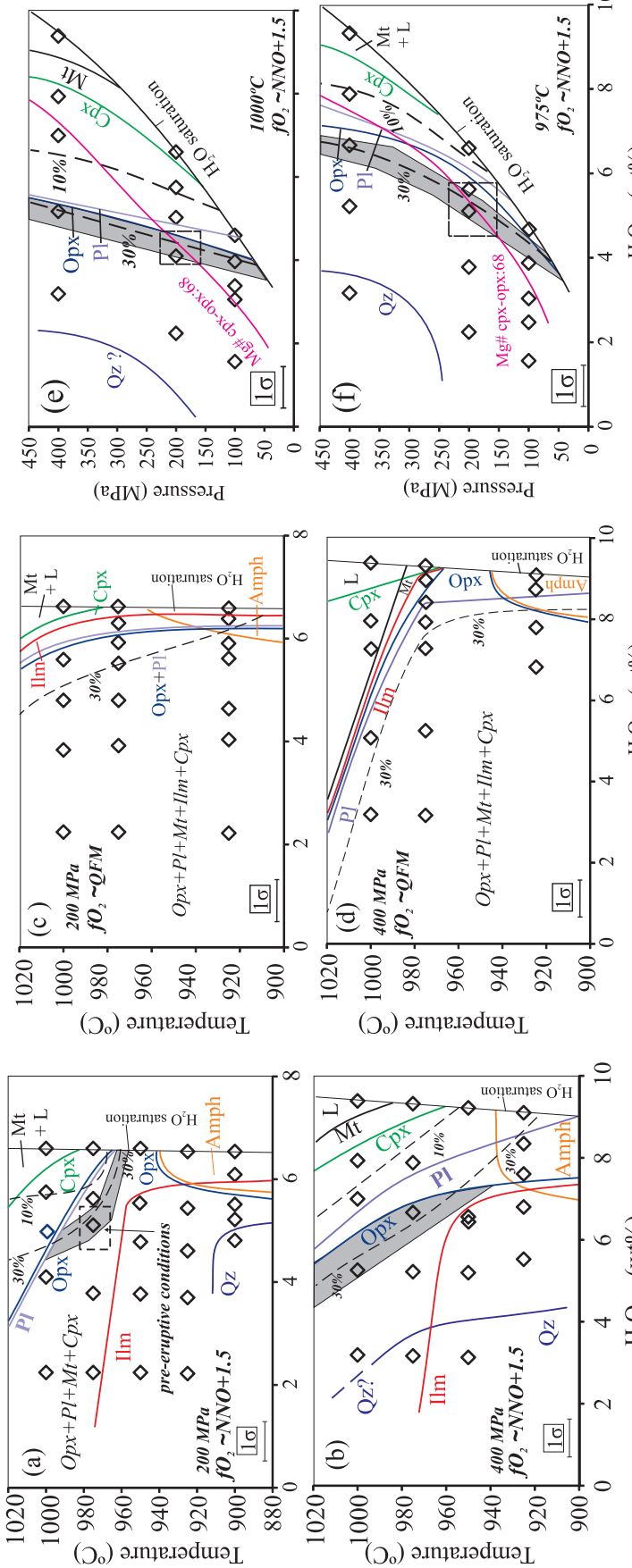

Fig. 3. Phase relationships of the Upper Scoriae 1 andesite at (a) 200 MPa and $fO_2 \sim$ NNO + 1·5, (b) 400 MPa and $fO_2 \sim$ NNO + 1·5, (c) 200 MPa and $fO_2 \sim$ QFM, (d) 400 MPa and $fO_2 \sim$ QFM, (e) 1000 °C and $fO_2 \sim$ NNO + 1·5, and (f) 975 °C and $fO_2 \sim$ NNO + 1·5 for various temperatures, pressures and water contents in the melt. L, liquid; Pl, plagioclase; Cpx, clinopyroxene; Opx, orthopyroxene; Amph, amphibole; Mt, magnetite; Ilm, ilmenite; Qz, quartz. Dashed lines are estimated crystal content boundaries (in wt %). Grey field in (a) and (b) shows the coexistence region of the natural mineral assemblage and 28 wt % of crystals in the andesite.

Crystal contents and phase proportions of experimental charges

The proportion of solid phases increases in a general way with decreasing H_2O_{melt} (at constant pressure), decreasing temperature (at constant H_2O_{melt}) and increasing pressure (at constant temperature and H_2O_{melt}; Supplementary Data crystal appendix). The highest value that we could determine by mass-balance calculation (71 wt %) is reached at 925°C, 400 MPa, NNO + 1·5 and 7 wt % H_2O_{melt}. A decrease in fO_2 from NNO + 1·5 to QFM at constant temperature, pressure and H_2O_{melt} decreases the crystal content (975°C, 200 MPa series; Supplementary Data crystal appendix; Table 2). Mt and Cpx proportions increase slightly with decreasing H_2O_{melt} or temperature to a maximum of 20 wt % (Table 2). Pl rapidly becomes the dominant mineral when present (Table 2). Opx and Ilm appear in lower amounts compared with Cpx and Mt (on average <3 wt % for Opx and <1 wt % for Ilm). Under oxidizing conditions and similar H_2O_{melt} contents, the proportion of Amph depends on pressure: charges annealed at 200 MPa have about 5 wt % Amph compared with >13 wt % at 400 MPa (Table 2). Charges annealed at similar T, P and H_2O_{melt} but lower fO_2 crystallize less Mt and more Cpx and Opx, whereas the Pl proportion remains almost constant when compared with more oxidized runs.

Mineral compositions

Plagioclase

The compositional variation of Pl (An mol %, Or mol %) as a function of H_2O_{melt} and temperature is shown in Fig. 4. Pl composition is in the range $An_{37–70}Ab_{30–55}Or_{0·4–9·4}$ (Table 3), being mostly affected by changes in temperature, H_2O_{melt}, and pressure. The most calcic Pl (An_{70}) is produced at 925°C, 200 MPa, 6·5 wt % H_2O_{melt}, whereas the least calcic Pl (An_{37}) is produced at 950°C, 400 MPa, 5 wt % H_2O_{melt}, both under oxidizing conditions. At a given pressure, the An content decreases and Or content increases with the decrease in H_2O_{melt} and temperature (Fig. 4), mirroring the decrease of the CaO/K_2O ratio of the coexisting melt as crystallization proceeds (see below). The effect is well illustrated by the experimental series annealed at 200–400 MPa and oxidizing conditions in which a decrease of 2 wt % H_2O_{melt} or a change in temperature from 1000–975°C to 950–925°C decreases by 10–15 mol % the An content of Pl (Fig. 4). At fixed temperature increasing either H_2O_{melt} or fO_2, or decreasing pressure, all increase the An content. For example, in the series annealed under oxidizing conditions, 1000–975°C and for H_2O_{melt} of 4–5 wt %, the An content increases from An_{47} to An_{68} when pressure decreases from 400 to 100 MPa. Changes in fO_2 produce modest compositional variations of Pl compared with those of pressure: a decrease in fO_2 from NNO + 1·5 to QFM at a given pressure and H_2O_{melt} decreases An content by about 5 mol % (Fig. 4). The Pl–liquid Ca–Na exchange K_d varies between 0·19 and 3·21 with an average value of 1·78 (± 0·7), being in good agreement with previous studies on hydrous basaltic–andesitic compositions (Table 3; Baker & Eggler, 1987; Sisson & Grove, 1993; Pichavant *et al.*, 2002; Berndt *et al.*, 2005; Grove *et al.*, 2005; Di Carlo *et al.*, 2006).

Pl compositional changes as a function of temperature, H_2O_{melt}, per cent crystals and fO_2 have been parameterized using a linear least-squares fitting procedure. We have not considered adding a pressure term to this equation because of the limited range of P variation covered in this work. The following empirical equation has been derived:

$$\mathrm{An(mol\ \%)} = 0\cdot006T(^\circ\mathrm{C}) - 0\cdot7\mathrm{H_2O_{melt}} + 2\cdot72\Delta\mathrm{NNO} - 0\cdot32(\mathrm{wt\ \%\ crystals}) + 60\cdot22 \quad (1)$$

for which $R^2 = 0·91$ (see Supplementary Data Appendix Equations).

Equation (1) can be used to allow back-calculation of experimental An contents to within ±1·5 mol %. Owing to its empirical nature, we caution the use of such an equation on compositions significantly different from that of the USC-1 sample. Equation (1) (and those following) is applicable in the range 1000–900°C, H_2O_{melt} 10 to 1 wt % and $fO_2 \sim$ NNO + 1·5 to QFM.

Clinopyroxene

Experimental Cpx is either augite or diopside according to the classification of Morimoto (1989) with compositions in the range $En_{37–47}Fs_{13–39}Wo_{17–48}$, Mg#49–77, with TiO_2 and Al_2O_3 contents in the range 0·4–1·7 wt % and 1·3–8 wt %, respectively (Table 4, Fig. 5; Supplementary Data Appendix cpx). Cpx composition varies with changes in experimental parameters, and hence with crystal content and melt composition. At constant temperature a decrease in H_2O_{melt} from 6 to 3 wt % decreases the Mg# and Wo by about 10%. Similar changes are produced by an increase in pressure from 200 to 400 MPa or by an fO_2 decrease from NNO + 1·5 to QFM. In contrast, changes in temperature at constant pressure have smaller effects (<5 mol %), except when temperature decreases from 950°C to 900°C (>15 mol % in series at 200 MPa, NNO + 1·5). Overall, Cpx becomes progressively poorer in Al_2O_3 and TiO_2 when H_2O_{melt} decreases (i.e. with increase in crystallization) and with decreasing fO_2 (Supplementary Data appendix cpx). The $K_d^{Fe/Mg}$ of Cpx–liquid pairs ranges between 0·12 and 0·26 (average 0·22 ± 0·05), again in agreement with previous experimental studies conducted on similar compositions (Table 4; Pichavant *et al.*, 2002; Berndt *et al.*, 2005; Di Carlo *et al.*, 2006).

The variation of Wo content with experimental conditions can be parameterized using a linear least-squares procedure on the entire experimental database:

$$\mathrm{Wo(mol\ \%)} = -0\cdot0075T(^\circ\mathrm{C}) + 1\cdot36\mathrm{H_2O_{melt}(wt\ \%)} + 3\cdot76\Delta\mathrm{NNO} + 35\cdot16 \quad (2)$$

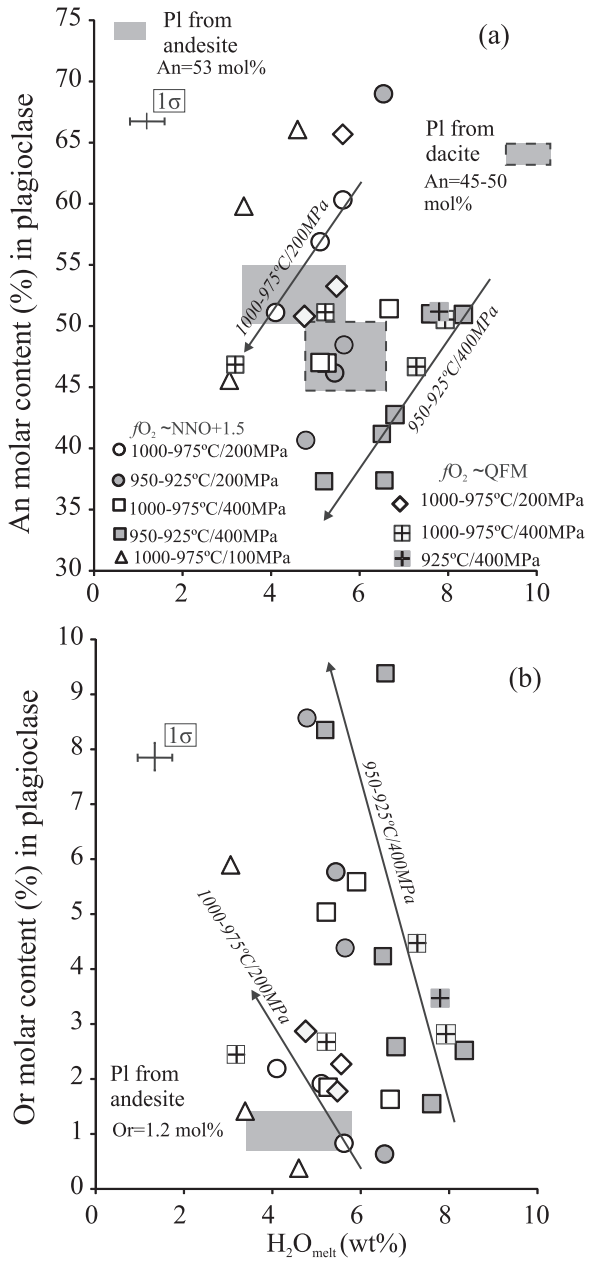

Fig. 4. Compositional variation of the experimental plagioclase. (a) An content (mol %) vs H_2O_{melt} (wt %); (b) Or content (mol %) vs H_2O_{melt} (wt %). Numbers next to symbols in the legend indicate temperature (°C) and pressure (MPa) at specified fO_2 conditions. Grey box indicates the plagioclase composition of the natural andesite phenocrysts and dashed grey box indicates that for the dacite xenocrysts [see text for details, and Andújar *et al.* (2015)].

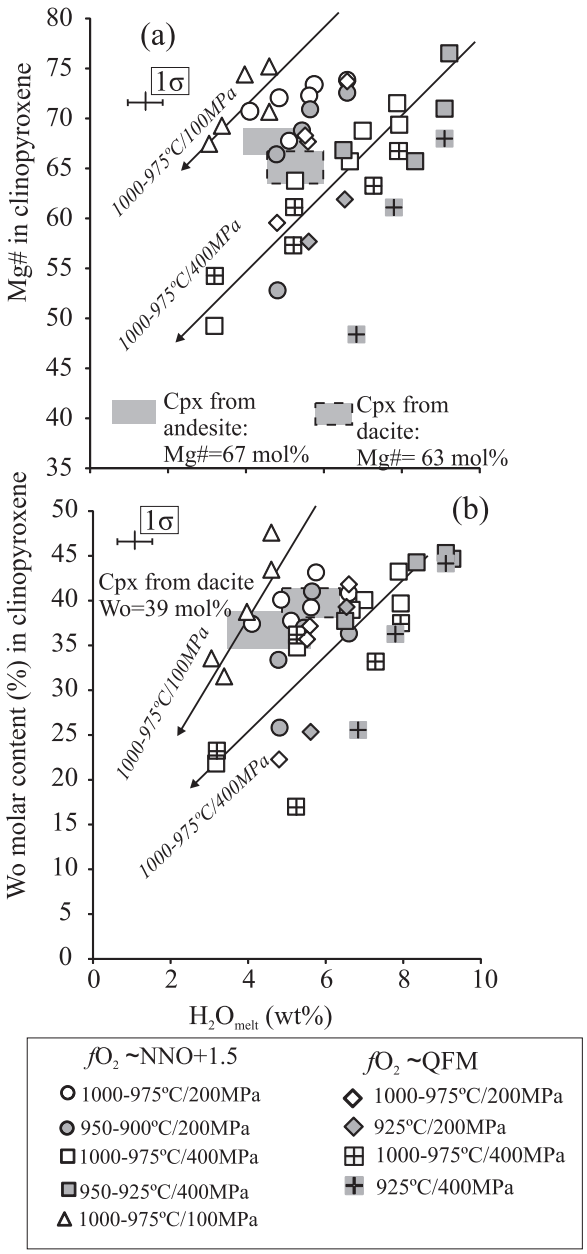

Fig. 5. Compositional variation of experimental clinopyroxenes. (a) Mg# and (b) Wo content of clinopyroxenes as functions of melt H_2O. Numbers next to symbols in the legend indicate temperature (°C) and pressure (MPa) at specified fO_2 conditions. Grey box represents the clinopyroxene composition of the natural andesite phenocrysts and dashed grey box indicates that for the dacite xenocrysts [see text for details, and Andújar *et al.* (2015)].

for which $R^2 = 0{\cdot}86$ (Supplementary Data Appendix Equations).

Equation (2) can be used to back-calculate observed Wo contents to within ±0·8 mol %.

Orthopyroxene

According to the classification of Morimoto (1989) experimental Opx is clinoenstatite–pigeonite with compositions in the range $En_{51–71}Fs_{24–44}Wo_{3·5–16}$, Mg#49–75, with 1–5 wt % Al_2O_3 and 0·2–0·6 wt % TiO_2 (Table 5).

The variation of H_2O_{melt} significantly affects Opx composition: for instance, a decrease of 2 wt % H_2O_{melt} decreases by 5–8 mol % the Mg# (and the Fs component) whereas the Wo content is slightly affected (Fig. 6a). Compositional changes owing to temperature variation are modest in the range 1000–950°C, but more important below 950°C: Mg# and En decrease by 5–15 mol % when temperature decreases from 950 to 900 °C (Fig. 6). In addition to temperature and water content effects, our results show that Opx composition is sensitive to

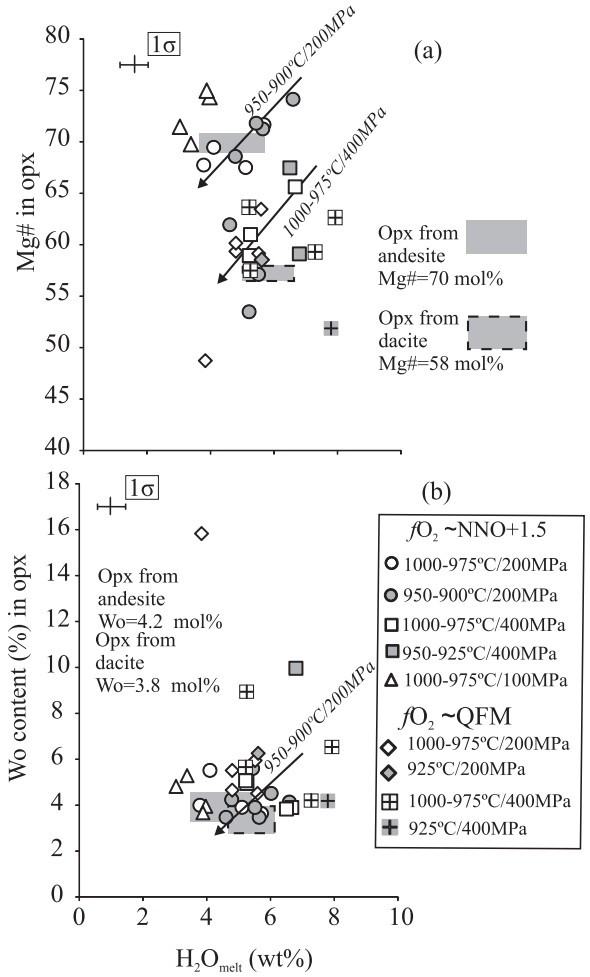

Fig. 6. Compositional variation of experimental orthopyroxenes. (a) Mg# and (b) Wo content of orthopyroxenes as a function of melt H_2O. Numbers next to symbols in the legend indicate temperature (°C), pressure (MPa) and fO_2 conditions. Grey box represents the orthopyroxene composition of the natural andesite phenocrysts and dashed grey box indicates that for the dacite xenocrysts [see text for details, and Andújar *et al.* (2015)].

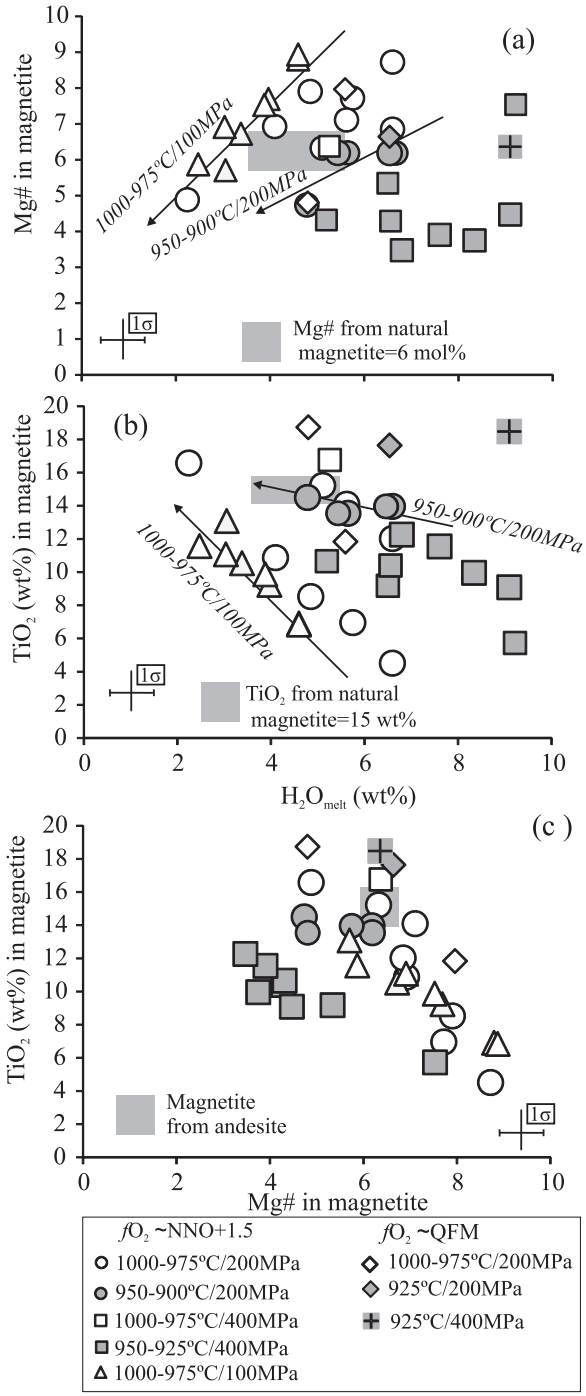

Fig. 7. Compositional variation of experimental magnetites. (a) Mg# and (b) TiO_2 (wt %) content as function of melt H_2O. (c) TiO_2 (wt %) content as a function of Mg# of magnetite. The grey square shows the magnetite population found in the USC-1 andesite sample.

pressure variation at oxidizing conditions; for a constant H_2O_{melt} and fixed temperature the increase in pressure from 100 to 400 MPa increases Mg# and the En content by about 15–20 mol %. The change in fO_2 from NNO + 1·5 to QFM produces compositional changes similar to those of H_2O_{melt}, in particular at 200 MPa. The effect of experimental parameters on Wo content (and Al_2O_3 and TiO_2, not shown) is small, with most Opx clustering in the range $Wo_{4–6}$. The Opx–liquid Fe/Mg exchange K_d varies between 0·11 and 0·29 (Table 5) and has an average value of 0·21 ± 0·05.

Magnetite and ilmenite

Mt has a FeO* content between 59 and 79 wt % and a TiO_2 content from 5 to 19 wt % (Table 6). The Mg# [calculated as Mg# = 100Mg/(Mg + Fe_{tot}) on a stoichiometric basis] varies between 3·5 and 9% (Table 6; Fig. 7). As for other phases, changes in experimental parameters do affect Mt composition. A decrease in temperature and fO_2 produces moderate variations of Mg# and TiO_2 content (2–4%). The effect of H_2O_{melt} is significant as well: a decrease of 3 wt % H_2O_{melt} at constant temperature decreases Mg# by 5% and increases TiO_2 up to 12 wt % (e.g. series at 1000°C, 200 MPa and 950°C,

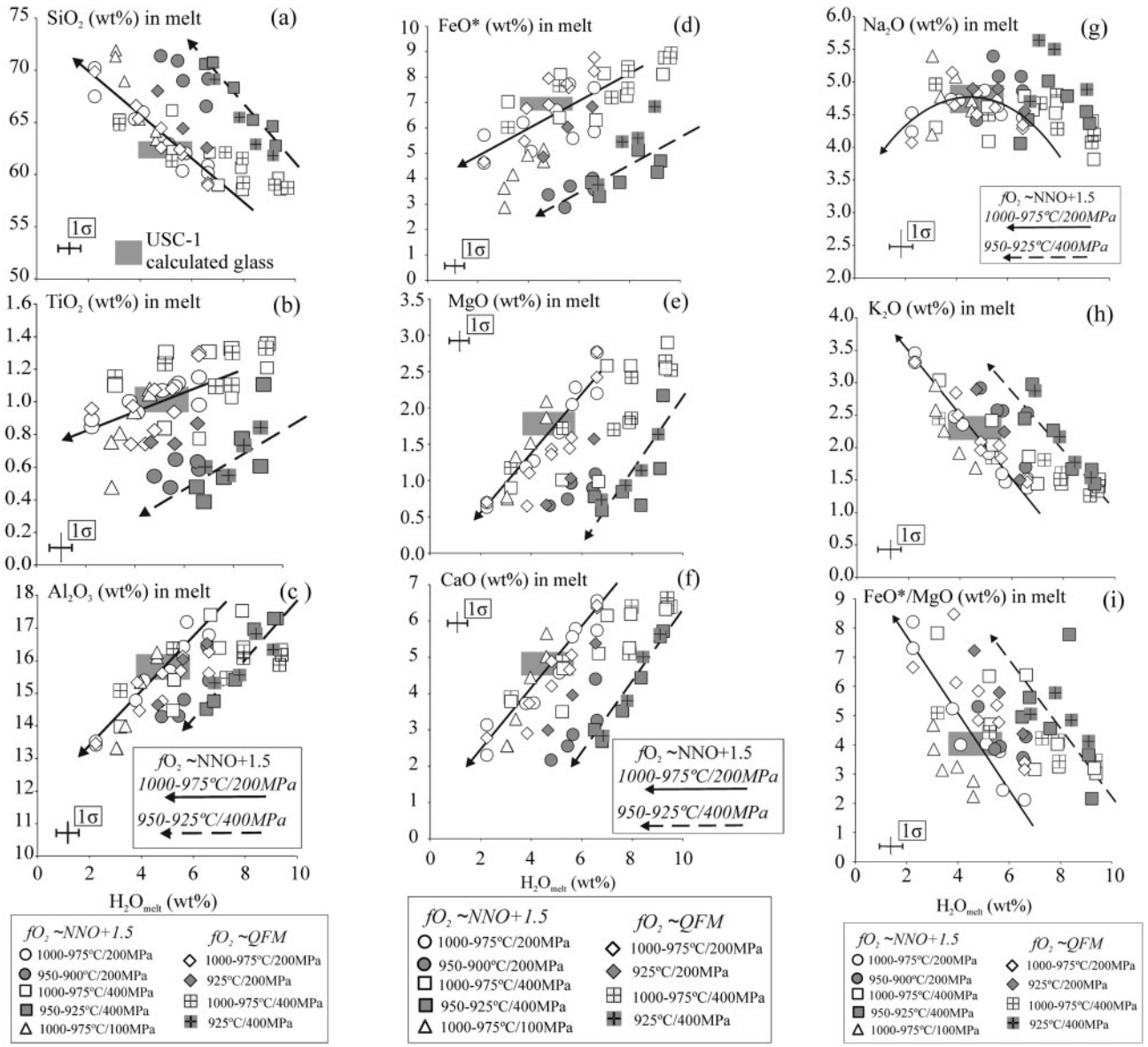

Fig. 8. (a–i) Experimental glass compositional variations of major and minor oxides and FeO*/MgO with water content in the melt. Grey horizontal bar shows the natural USC-1 andesite calculated melt composition (Table 1).

400 MPa; Fig. 7). At fixed T, H_2O_{melt} and fO_2, a pressure increase from 100 to 400 MPa decreases the Mg# by 2–4%. The effect on TiO_2 content is less clear compared with that on Mg# (Fig. 7).

We have linearly regressed the compositional variations of Mg# in magnetite with T, H_2O_{melt}, crystal content (wt %) and fO_2, and obtained the following empirical equation:

$$\begin{aligned} \mathrm{Mg\#_{magnetite}(mol\ \%)} = {} & 0\cdot027T + 0\cdot28\mathrm{H_2O_{melt}(wt\ \%)} \\ & - 0\cdot024(\mathrm{wt\ \%\ crystals}) \\ & + 0\cdot40\Delta\mathrm{NNO} - 20\cdot62 \end{aligned} \quad (3)$$

for which $R^2 = 0{\cdot}82$ (see Supplementary Data Appendix Equations).

Equation (3) allows back-calculation of observed Mg# in magnetites to within ±0·7.

Ilm was identified by scanning electron microscope–energy-dispersive spectrometry (SEM-EDS) in several charges but was often too small to obtain reliable compositions by electron microprobe. Nevertheless, we analysed Ilm in seven charges annealed at QFM (Table 7). Their FeO* and TiO_2 contents are in the range 40–45 wt % and 48–50 wt %, respectively. The limited amount of data prevents quantification of the effect of experimental parameter variation on Ilm composition.

Amphibole

According to the classification of Leake *et al.* (1997), experimental Amph is ferro-tschermakite to pargasitic

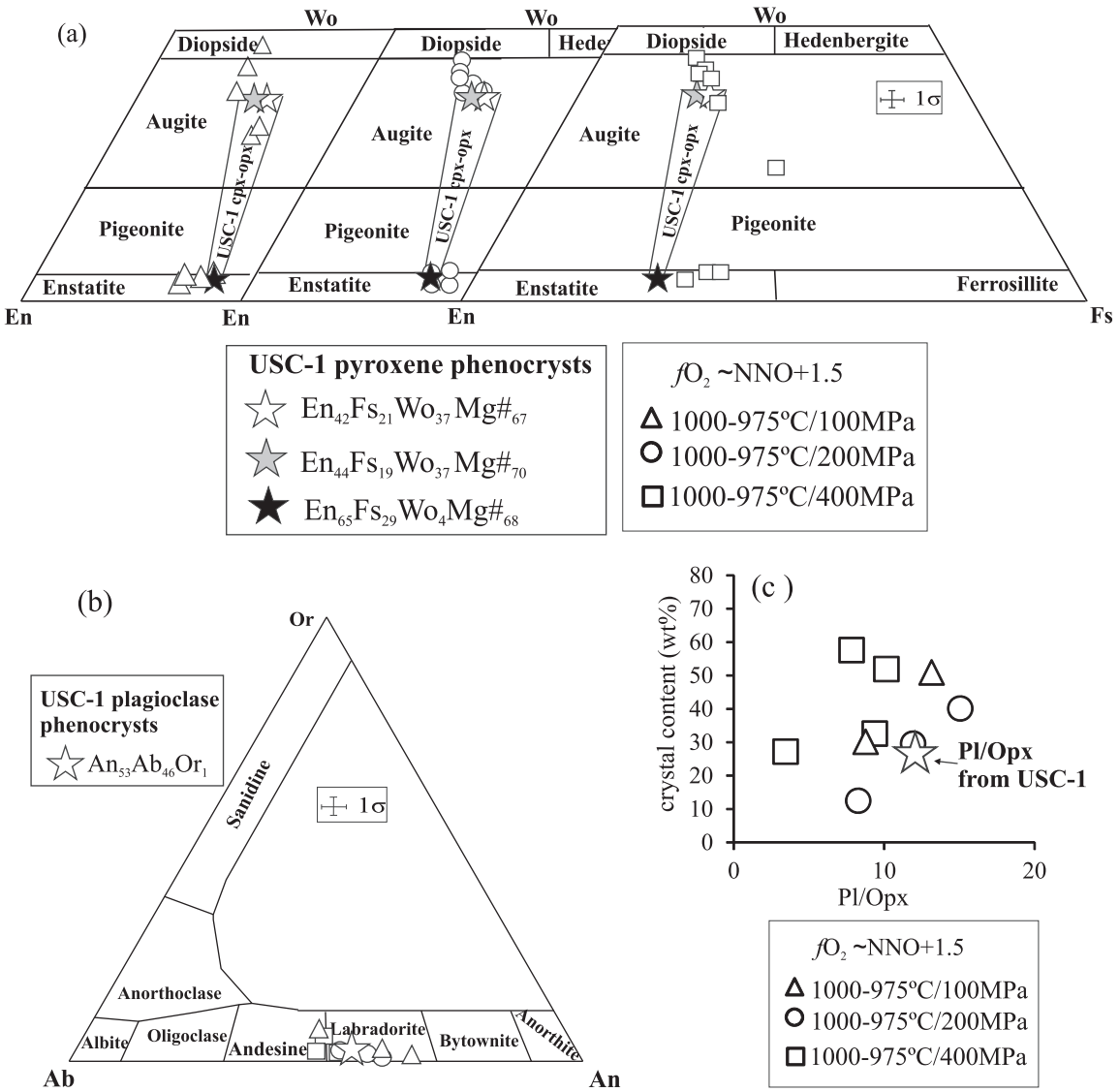

Fig. 9. (a) Compositions of clinopyroxenes and orthopyroxenes of USC-1 (Andújar *et al.* 2015; this work) and those from runs at fO_2 ~ NNO + 1·5, 1000–975 °C, and 100, 200 and 400 MPa plotted onto the classification scheme of Morimoto (1989); tie-lines for the main cpx–opx populations from the andesite are shown. (b) Compositions of plagioclase of USC-1 (Andújar *et al.*, 2015, this work) and those from experiments plotted using the classification scheme of Deer *et al.* (1972). (c) Crystal content as a function of plagioclase/orthopyroxene ratio (Pl/Opx) of experiments reproducing the crystal content and mineral assemblage (a, b) of the natural andesite (white star).

hornblende. Its Mg# (calculated with FeO*) shows limited variability with changes in H_2O_{melt}, fO_2 or pressure (Table 8; Supplementary Data Amphibole Appendix). Similarly, Amph crystallizing at 400 MPa has an Al(IV) content comparable with, or slightly higher than, that at 200 MPa, showing that any pressure effect on Amph composition is minor in the 200–400 MPa interval.

Residual glass

Experimental glasses (Table 9) range from andesitic (58·5 wt % SiO_2) to dacitic (63–68 wt % SiO_2) to rhyodacitic (up to 72 wt % SiO_2) compositions, with some charges straddling the trachyandesite–trachydacite boundary (e.g. charges usc30, usc34) based on the criteria of Le Bas & Streckeisen (1991). The observed melt evolution arises obviously from changes in phase assemblages, proportions and compositions: mostly Fe–Mg minerals (Cpx–Opx mainly and Mt) and Pl, as well as the incipient crystallization of Amph or Ilm at lower temperatures (950–925°C). The experimental trends reproduce the typical evolution of arc andesites (Table 2; Martel *et al.*, 1999; Pichavant *et al.*, 2002; Almeev *et al.*, 2013). In detail, glass composition varies mostly with H_2O_{melt} (or increasing crystal content), and less so with *T*, *P* and fO_2 (Fig. 8): a decrease of 3–4 wt % H_2O_{melt} decreases TiO_2, Al_2O_3, FeO*, MgO and CaO content by

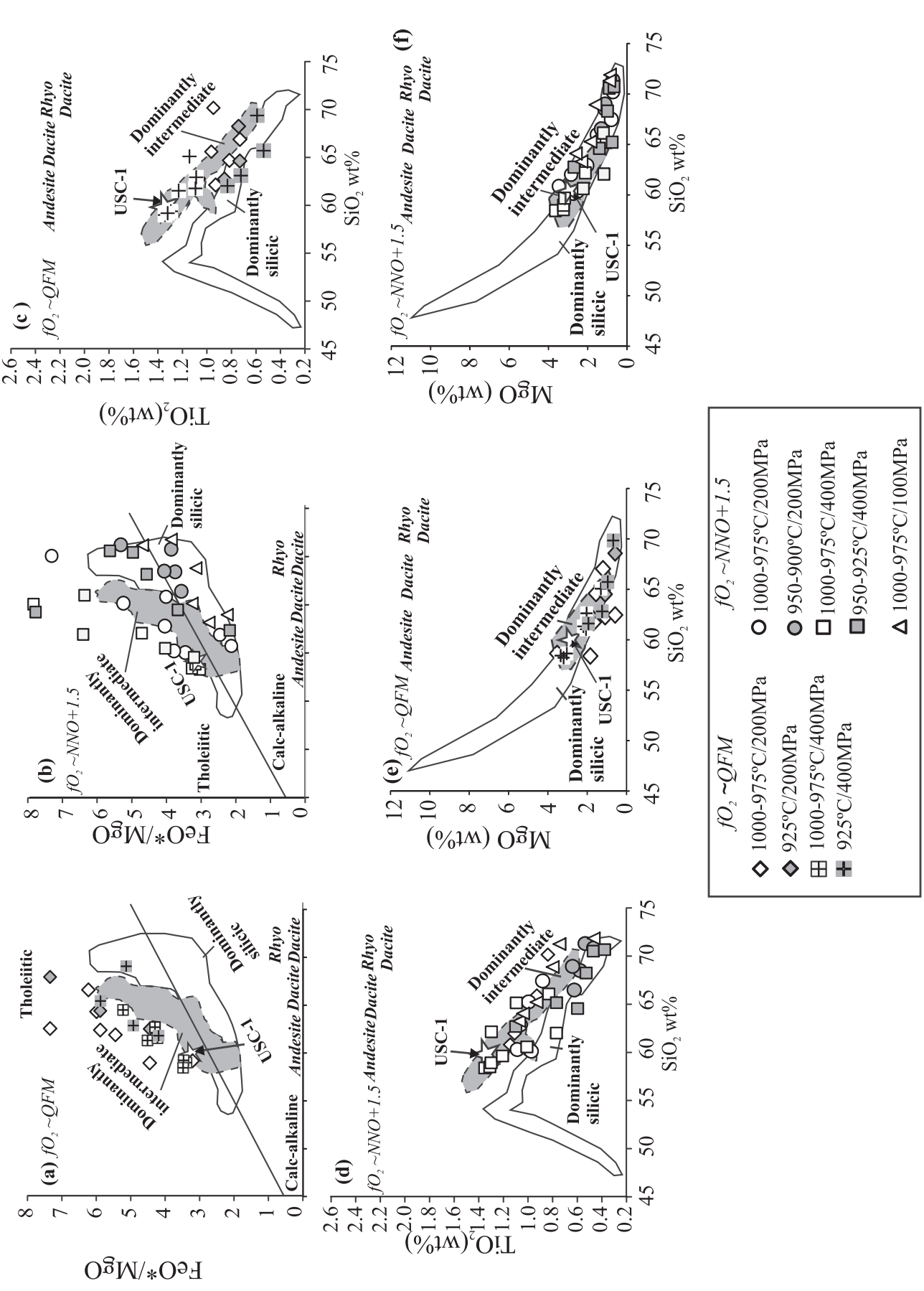

Fig. 10. (a, b) FeO*/MgO and (c, d) TiO_2 vs SiO_2, and tholeiitic and calc-alkaline affinities of Santorini magmas (silicic- and intermediate-dominated compositions); (e, f) MgO vs SiO_2 (wt %) of Santorini magmas and experimental melts at $fO_2 \sim$ QFM and NNO + 1·5. Natural rock data from Druitt *et al.* (1999). Errors are equal to symbol size.

Table 3: Experimental plagioclase composition (wt %)

Run	*n*	SiO_2	TiO_2	Al_2O_3	MgO	CaO	MnO	FeO*	Na_2O	K_2O	Sum	An	Ab	Or	$K_d^{Ca–Na}$
Oxidized experiments															
1000°C, 200 MPa															
usc65	1	55·43	0·08	25·80	0·16	10·00	0·00	1·07	5·05	0·36	97·95	51·11	46·70	2·19	0·19
975°C, 200 MPa															
usc32															
usc33	1	53·60	0·05	28·42	0·10	12·13	0·03	1·18	4·32	0·14	99·95	60·31	38·86	0·83	1·63
usc34	1	55·07	0·19	26·38	0·26	10·62	0·00	1·05	4·25	0·30	98·11	56·89	41·20	1·91	1·95
950°C, 200 MPa															
usc53	2	57·49	0·25	26·43	0·21	8·79	0·04	1·38	4·73	0·67	100·00	48·46	47·16	4·38	2·29
SD		0·40	0·04	0·08	0·01	0·06	0·04	0·13	0·07	0·05	0·76	0·68	0·40	0·28	
usc54	1	61·37	0·24	20·43	0·48	6·46	0·00	1·66	4·46	1·14	96·25	40·66	50·77	8·57	2·06
925°C, 200 MPa															
usc42	3	50·13	0·05	29·46	0·18	13·93	0·05	0·70	3·39	0·11	98·00	68·98	30·38	0·63	3·22
SD		0·39	0·02	0·47	0·18	0·72	0·05	0·17	0·07	0·02	0·69	1·46	1·52	0·14	
usc43	1	57·43	0·21	23·82	0·47	7·95	0·00	1·74	4·57	0·83	97·03	46·16	48·07	5·77	2·79
1000°C, 400 MPa															
usc70	1	56·04	0·15	26·35	0·10	9·55	0·00	1·16	5·75	0·32	99·43	46·97	51·18	1·85	0·88
975°C, 400 MPa															
usc39	1	58·22	0·33	25·96	0·13	9·03	0·57	0·96	4·56	0·24	100·00	51·42	46·95	1·63	1·48
usc40	1	60·35	0·29	23·79	0·54	8·89	0·05	0·27	5·01	0·80	100·00	47·02	47·95	5·04	1·55
950°C, 400 MPa															
usc78	2	58·69	0·19	24·27	0·25	7·77	0·06	1·29	5·69	0·67	97·90	41·17	54·60	4·23	1·06
SD		0·42	0·11	0·89	0·16	0·28	0·09	0·19	0·01	0·01	0·35	0·97	0·82	0·15	
usc79	1	60·59	0·14	20·84	0·27	6·25	0·03	1·83	4·92	1·32	96·20	37·37	53·25	9·38	
usc80	1	60·85	0·32	21·30	0·28	6·43	0·08	1·49	5·18	1·21	97·13	37·30	54·35	8·35	
925°C, 400 MPa															
usc83	1	58·57	0·09	25·03	0·10	9·63	0·00	0·80	4·86	0·40	99·48	50·95	46·53	2·52	1·52
usc84	1	58·61	0·07	26·69	0·05	10·19	0·00	0·96	5·24	0·26	102·07	51·00	47·45	1·55	1·77
usc85	1	61·02	0·21	24·61	0·07	8·07	0·11	1·15	5·70	0·41	101·35	42·76	54·65	2·59	1·36
1000°C, 100 MPa															
usc72	1	51·79	0·03	29·82	0·04	13·18	0·00	1·02	3·70	0·06	99·65	66·06	33·56	0·38	2·11
usc74	1	57·92	0·04	26·01	0·14	10·94	0·00	0·97	3·92	0·22	100·15	59·80	38·79	1·41	2·67
usc75	1	59·56	0·29	23·23	0·47	7·74	0·00	1·89	4·56	0·84	98·58	45·56	48·54	5·90	2·77
Reduced experiments															
1000°C, 200 MPa															
usc28	1	53·24	0·26	29·81	0·25	12·45	0·17	0·08	3·38	0·35	100·00	65·58	32·25	2·17	2·52
975°C, 200 MPa															
usc2	2	56·04	0·02	27·24	0·84	10·85	0·11	0·05	5·10	0·30	100·55	53·10	45·16	1·75	1·36
SD		1·85	0·00	0·93	0·03	0·23	0·02	0·14	0·25	0·02	2·08	0·65	0·61	0·04	
usc3	3	55·54	0·24	25·15	0·41	9·89	0·07	1·81	5·03	0·46	98·61	50·63	46·54	2·83	1·25
SD		0·97	0·13	1·14	0·07	0·50	0·04	0·38	0·27	0·07	0·79	0·18	0·36	0·53	
1000°C, 400 MPa															
usc25	1	55·34	0·29	25·74	0·30	9·66	0·00	1·20	4·82	0·42	97·77	51·13	46·20	2·67	1·35
usc26	1	57·15	0·13	26·56	0·33	9·25	0·04	1·04	5·53	0·41	100·44	46·85	50·71	2·44	1·43
975°C, 400 MPa															
usc12	1	56·53	0·16	26·76	0·51	9·59	0·04	1·74	4·89	0·45	100·67	50·53	46·65	2·82	1·37
usc13	1	57·68	0·30	25·14	0·41	7·99	0·01	1·70	4·62	0·64	98·49	46·67	48·85	4·47	1·32
925°C, 400 MPa															
usc89	2	58·08	0·21	24·49	0·22	9·09	0·04	1·02	4·45	0·52	98·11	51·18	45·35	3·47	2·57
SD		1·10	0·01	0·59	0·07	0·16	0·05	0·04	0·22	0·01	1·25	0·69	0·88	0·20	

n, number of analysis; SD, standard deviation. FeO*, total iron reported as FeO. An = 100Ca/(Ca + Na + K); Ab = 100Na/(Ca + Na + K); Or = 100K/(Ca + Na + K). End-members calculated as done by Deer et al. (1972). $K_d^{Ca–Na}$ = (Ca/Na in plagioclase)/(Ca/Na in melt).

about 20–50% relative, whereas both SiO_2 and K_2O increase (Fig. 8). Na_2O displays a different behaviour compared with other oxides, first increasing until H_2O_{melt} reaches 6 wt %, then decreasing upon further reduction of H_2O_{melt} (Fig. 8g). Glasses from charges annealed either in the range 1000–975°C or in the range 950–925°C define two distinct trends (Fig. 8). The compositional differences between these two groups are clear for SiO_2, TiO_2, FeO*, MgO and CaO oxides, being less pronounced for Na_2O, K_2O and Al_2O_3 (5–10% relative). This thermal and compositional divide at ~965°C is related to the onset of ilmenite crystallization and the increase in the modal proportion of plagioclase (Fig. 3; Table 2), which accelerates and enhances subsequent melt evolution. An increase in pressure from 100 to 400 MPa at constant temperature produces moderate changes in melt composition, of the order of 1–2 wt % on major oxides. However, a larger pressure effect on melt composition is apparent when the FeO*/MgO ratio is considered (with an average precision of ± 0·5; Table 9). Glasses at 100 MPa have the lowest ratios, and those at 400 MPa the highest, whereas those at 200 MPa plot

Table 4: Composition of experimental clinopyroxenes (wt %)

	n	SiO_2	TiO_2	Al_2O_3	MgO	CaO	MnO	FeO*	Na_2O	K_2O	Total	En	Fs	Wo	Mg#	K_d^{Fe*-Mg}
Oxidized experiments																
1000°C, 200 MPa																
usc63	3	47·50	1·43	5·36	13·67	19·95	0·46	8·84	0·37	0·04	97·61	41·14	14·92	43·15	73·39	0·26
SD		0·38	0·05	0·13	0·05	0·10	0·04	0·39	0·11	0·05	0·27	0·06	0·58	0·45	0·79	
usc64	1	47·30	1·22	4·54	14·24	18·57	0·32	9·84	0·56	0·06	96·64	42·77	16·58	40·10	72·06	
usc65	1	50·22	0·64	2·35	15·71	18·79	0·67	11·60	0·02	0·00	100·00	43·52	18·03	37·40	70·71	0·18
975°C, 200 MPa																
usc32	3	51·02	0·66	3·68	14·87	19·50	0·34	9·38	0·46	0·12	100·01	43·28	15·32	40·84	73·85	0·18
SD		0·52	0·10	1·16	0·94	0·60	0·13	0·46	0·15	0·10	0·75	0·68	0·44	0·78	0·76	
usc33	4	50·78	0·77	3·43	15·44	19·40	0·42	10·55	0·36	0·02	101·18	43·44	16·66	39·24	72·28	0·18
SD		0·10	0·10	0·21	0·30	0·60	0·07	0·25	0·11	0·03	0·67	0·75	0·47	1·08	0·37	
usc34	3	51·60	0·77	3·97	14·41	18·18	0·47	12·22	0·63	0·14	102·39	41·65	19·82	37·76	67·76	0·21
SD		0·39	0·35	0·75	0·41	0·35	0·19	0·38	0·14	0·07	0·50	0·52	0·93	0·12	1·29	
950°C, 200 MPa																
usc52	1	52·65	0·48	2·93	15·24	17·09	0·94	10·27	0·47	0·06	100·12	45·07	17·04	36·32	72·57	0·18
usc53	1	52·78	0·44	3·00	13·90	19·23	0·45	10·17	0·03	0·00	100·00	41·28	16·94	41·03	70·91	0·19
usc54	2	51·88	0·49	2·88	14·71	15·77	0·75	13·28	0·24	0·00	100·00	43·38	21·98	33·39	66·41	0·17
SD		0·39	0·03	0·33	0·07	1·78	0·16	0·87	0·07	0·00	0·00	0·79	1·93	3·01	1·56	
925°C, 200 MPa																
usc43	1	50·36	0·57	2·76	15·05	18·27	0·88	12·17	0·00	0·00	100·00	42·39	19·23	36·98	68·79	0·17
900°C, 200 MPa																
usc61	1	48·80	0·96	1·30	12·47	11·63	0·73	19·87	0·20	0·05	96·01	38·50	34·41	25·81	52·80	
1000°C, 400 MPa																
usc68	3	48·88	1·11	4·74	13·83	18·51	0·50	10·88	0·56	0·05	99·05	41·25	18·22	39·69	69·37	0·24
SD		0·61	0·09	0·28	0·38	0·66	0·04	0·30	0·07	0·02	0·47	0·45	0·86	0·64	1·18	
usc69	2	49·00	0·90	4·56	13·63	18·63	0·40	11·03	0·57	0·06	98·79	40·74	18·51	40·06	68·77	0·26
SD		0·09	0·03	0·03	0·31	0·14	0·22	0·47	0·00	0·03	0·48	0·52	0·59	0·72	0·42	
usc70	1	50·27	0·79	3·53	13·35	15·62	0·25	13·51	0·52	0·04	97·88	41·32	23·47	34·77	63·77	0·34
usc71	2	49·74	0·71	2·10	12·17	10·29	0·80	22·35	0·27	0·07	98·49	37·38	38·52	22·71	49·25	0·24
SD		0·42	0·08	0·23	0·33	0·46	0·12	0·28	0·08	0·01	0·92	0·76	0·21	1·18	0·37	
975°C, 400 MPa																
usc38	1	48·76	0·82	5·21	13·01	19·48	0·33	9·24	0·54	0·07	97·46	40·19	16·00	43·23	71·52	0·18
usc39	1	50·34	0·68	2·76	13·86	18·98	0·48	12·90	0·00	0·00	100·00	39·59	20·66	38·96	65·71	0·15
950°C, 400 MPa																
usc77	3	48·99	0·96	4·22	14·20	20·98	0·20	7·78	0·46	0·06	97·85	42·07	12·93	44·67	76·50	0·25
SD		0·45	0·13	0·11	0·14	0·17	0·18	0·50	0·03	0·06	0·38	0·27	0·63	0·68	0·98	
usc78	3	51·50	0·61	5·86	12·44	16·03	0·75	11·02	1·22	0·15	99·59	40·68	20·20	37·73	66·82	0·16
SD		0·76	0·08	2·58	0·96	0·82	0·24	1·18	0·80	0·04	0·89	0·02	0·60	0·97	0·65	
925°C, 400 MPa																
usc82	2	52·35	0·58	2·70	13·31	21·89	0·42	9·71	0·36	0·03	101·34	38·33	15·68	45·31	70·97	0·20
SD		0·38	0·08	0·06	0·07	0·16	0·01	0·04	0·02	0·04	0·57	0·03	0·04	0·05	0·03	
usc83	1	52·30	0·90	5·06	12·10	20·51	0·26	11·25	0·62	0·11	103·11	36·33	18·95	44·27	65·72	0·12
1000°C, 100 MPa																
usc72	4	47·35	1·59	5·41	11·87	21·40	0·25	8·79	0·39	0·03	97·09	36·71	15·25	47·59	70·66	0·27
SD		0·20	0·13	0·33	0·23	0·19	0·08	0·48	0·04	0·05	0·83	0·55	0·78	0·42	1·35	
usc73	3	51·88	0·92	4·76	14·83	17·73	0·40	9·10	0·73	0·10	100·44	45·06	15·52	38·73	74·39	0·19
SD		0·63	0·18	0·18	0·42	0·16	0·00	0·35	0·08	0·02	0·39	0·71	0·42	0·54	0·74	
usc74	1	50·24	0·92	3·89	15·06	14·11	0·47	11·91	0·60	0·09	97·29	46·84	20·78	31·54	69·27	0·25
usc75	2	50·34	0·76	2·64	15·52	16·42	0·63	13·34	0·32	0·04	100·00	44·14	21·30	33·55	67·46	0·22
SD		0·47	0·08	1·36	0·17	1·19	0·02	0·24	0·19	0·01	0·00	0·65	0·92	1·56	0·63	
975°C, 100 MPa																
usc57b	1	47·22	1·69	5·66	13·93	20·16	0·59	8·19	0·31	0·05	97·81	41·77	13·78	43·45	75·20	0·26
Reduced experiments																
1000°C, 200 MPa																
usc28	2	52·70	0·94	3·72	14·34	17·31	0·42	12·88	0·31	0·13	102·72	42·02	20·08	37·16	67·67	0·19
SD		0·63	0·09	0·54	0·10	1·66	0·09	1·00	0·01	0·08	0·47	0·85	0·65	1·44	0·26	
usc29	1	52·73	0·43	1·81	16·02	10·86	0·61	19·40	0·20	0·04	102·10	45·70	31·05	22·27	59·55	0·25
975°C, 200 MPa																
usc1	4	48·88	0·90	2·96	14·90	20·41	0·38	9·47	0·25	0·04	98·19	42·44	15·14	41·81	73·71	0·20
SD		1·21	0·07	0·67	0·29	0·12	0·07	0·17	0·07	0·02	0·35	0·44	0·21	0·39	0·45	
usc2	2	49·93	0·89	3·78	14·58	16·74	0·57	12·08	0·45	0·07	99·09	43·25	20·10	35·68	68·28	0·15
SD		0·21	0·08	0·05	0·17	0·79	0·04	0·62	0·12	0·03	0·54	0·60	1·07	1·60	0·86	
925°C, 200 MPa																
usc6	1	51·10	0·75	7·72	10·05	14·75	0·24	11·03	1·17	0·39	0·39	37·26	22·94	39·29	61·89	0·25
usc7	1	49·87	0·45	3·17	13·65	11·34	0·60	17·86	0·40	0·07	97·41	42·44	31·15	25·35	57·67	0·22
1000°C, 400 MPa																
usc25	1	51·49	0·47	1·62	15·99	8·00	0·60	21·20	0·23	0·01	99·60	47·07	35·01	16·92	57·34	0·30
usc26	2	51·33	0·99	1·65	13·79	10·86	0·68	20·79	0·19	0·03	100·31	40·97	34·63	23·25	54·27	0·30
SD		0·69	0·47	0·07	0·55	2·19	0·01	2·82	0·03	0·00	1·50	0·95	4·13	5·07	2·38	

(continued)

Table 4. Continued

	n	SiO_2	TiO_2	Al_2O_3	MgO	CaO	MnO	FeO*	Na_2O	K_2O	Total	En	Fs	Wo	Mg#	$K_d^{Fe*–Mg}$
975°C, 400 MPa																
usc12	3	50·84	0·76	3·01	13·86	17·50	0·53	12·32	0·09	0·02	98·94	41·17	20·54	37·39	66·72	0·21
SD		0·36	0·08	0·49	0·81	0·84	0·07	0·67	0·15	0·03	1·84	0·33	0·10	0·17	0·21	
usc13	1	51·41	0·61	2·39	14·31	15·87	0·56	14·83	0·00	0·01	100·00	41·66	24·22	33·19	63·24	0·25
usc14	1	51·86	0·98	3·62	12·45	16·35	0·59	14·17	0·00	0·01	100·00	38·32	24·47	36·19	61·03	
925°C, 400 MPa																
usc87	2	51·11	0·69	3·18	12·39	20·23	0·30	10·40	0·31	0·06	98·66	37·61	17·72	44·15	67·97	0·20
SD		0·04	0·09	0·85	0·55	1·12	0·12	0·18	0·03	0·05	0·40	0·31	0·95	0·86	1·35	
usc89	1	51·26	0·65	3·32	12·22	16·06	0·50	13·88	0·47	0·15	98·50	38·39	24·46	36·26	61·08	0·23
usc90	1	51·61	0·62	4·55	10·62	10·66	0·65	20·19	0·47	0·20	99·56	35·42	37·79	25·56	48·38	

n, number of analysis; SD, standard deviation. FeO*, total iron reported as FeO. En, Fs and Wo were calculated as done by Morimoto (1989). Mg# = 100Mg/(Mg + Fe*). $K_d^{Fe*–Mg}$ = (Fe*/Mg in clinopyroxene)/(Fe*/Mg in melt).

between these, together defining three bands depending on pressure. This effect is enhanced at $fO_2 \sim$ NNO + 1·5 (Fig. 8; see below). A decrease in fO_2 from NNO + 1·5 to QFM produces melts richer in FeO* and slightly poorer in MgO and TiO_2, reflecting the overall low amounts of magnetite crystallizing in QFM charges (<2·0 wt %) and incoming of ilmenite (Table 2).

DISCUSSION

Storage conditions of Upper Scoriae 1 andesite

A first estimate of storage conditions of USC-1 can be retrieved from the comparison of the natural and experimental phase assemblages. The lack of Ilm in the andesite indicates that the fO_2 of the USC-1 magma is better approximated by the NNO + 1·5 experiments, as Ilm is always present in charges at QFM (Table 2, Fig. 3). At NNO + 1·5, Ilm crystallizes at ≤950°C, which fixes temperature in the range 975–1000°C. However, the isothermal sections in this temperature range (Fig. 3) show a large coexistence domain for the main mineral assemblage (Pl–Cpx–Opx–Mt), precluding any fine-tuning of pre-eruptive pressure using topological arguments alone. By considering the total crystal content of the natural andesite (28 wt %), a first estimate of H_2O_{melt} can be provided: at 975–1000°C, this amount of crystals is reproduced, together with the main mineral assemblage, at 4–7 wt % H_2O_{melt} in the pressure range 100–400 MPa (grey areas in Fig. 3).

This first estimate can be refined using the proportions and compositions of the minerals and glass (Figs 3–10). Considering an H_2O_{melt} range of 4–7 wt %, the *P*–*T*–H_2O_{melt} conditions that best approach the 28 wt % crystal content are 1000°C, 100 MPa, 4 H_2O_{melt} wt % or 1000–975°C, 200–400 MPa, 5–7 H_2O_{melt} wt %, respectively (Supplementary Data crystal content). Tighter constraints are provided when the crystal load (28 wt %), An content in Pl (53 mol %) and Mg# (68) of coexisting Cpx–Opx pairs are combined in isothermal–polybaric sections at 975–1000°C (Fig. 3e and f): these parameters define a *P*–H_2O_{melt} region (dashed-line squares in Fig. 3e and f) in the range 200 ± 40 MPa and 5 ± 0·5 wt % H_2O_{melt}, in which the characteristics of the natural andesite (at these temperatures) are best reproduced. Pressures as low as at 100 MPa can be ruled out because the compositions of the natural minerals are not reproduced at this pressure (see Figs 4–9). In contrast, charges annealed at 1000–975°C, 200 MPa and 4–5 H_2O_{melt} wt % successfully reproduce the Mg# and TiO_2 content of Mt, isolated augite phenocrysts ($En_{42}Fs_{21}Wo_{37}$, Mg#67 ± 1) and normally zoned Cpx crystals (cores of En_{44} $Fs_{19}Wo_{37}$, Mg#70 to rims of $En_{42}Fs_{21}Wo_{37}$, Mg#67 ± 1; see above), Opx ($En_{65}Fs_{29}Wo_4$Mg#68) and Pl (An_{53}) from the andesite (Figs 3–9). Charges annealed at 400 MPa, 1000–975°C and 5–7 wt % H_2O_{melt} also reproduce the natural Mt, Cpx and Pl compositions, but fail to reproduce the Mg#70 Cpx and Opx (it should be noted that Cpx–Opx crystals from these 400 MPa charges plot at 5–10 Mg#–Wo mol % lower compared with natural ones (Figs 5–9). In addition, when previous estimated conditions for the USC-1 andesite (*T*, *P*, fO_2, H_2O_{melt}) are used in equations (1)–(3), retrieved compositions for Mt (7·3 ± 0·4), Wo content in Cpx (38 ± 0·6 mol %) and An content in Pl (56 ± 0·3 mol %) match those of the natural sample (Table 1). These results support the validity of equations (1)–(3) for retrieving information about the ponding conditions of magmas having a composition similar to that of USC-1.

Further insights can be gained by using the experimental Pl/Opx ratio (wt %), which varies with crystallinity, temperature, pressure, H_2O_{melt} and fO_2 (Table 2; Fig. 9c). Because natural samples commonly contain antecrystic or xenocrystic minerals, the observed mineral modal proportions are not necessarily those of the mineral assemblage in equilibrium with the melt. Thus, to avoid the effect produced by the presence of foreign material, we use the crystal content (28 wt %) and a Pl/Opx ratio (12) calculated by mass balance using the phenocryst compositions in equilibrium with the andesitic magma (An_{53}, $En_{65}Fs_{19}Wo_4$; Table 1). In Fig. 9c the Pl/Opx ratio is plotted against the crystallinity of charges annealed at 100, 200 and 400 MPa. To achieve a given Pl/Opx ratio, charges at 200 MPa requires a lower degree of crystallization than at 400 MPa. Thus, considering the temperature interval 975–1000°C, charges

Table 5: Composition of experimental orthopyroxenes (wt %)

	n	SiO_2	TiO_2	Al_2O_3	MgO	CaO	MnO	FeO*	Na_2O	K_2O	Total	En	Fs	Wo	Mg#	$K_d^{Fe^*–Mg}$
Oxidized experiments																
1000°C, 200 MPa																
usc65	3	52·11	0·38	3·26	21·65	2·56	0·72	16·96	0·31	0·01	97·97	64·78	28·48	5·51	69·46	0·20
SD		0·54	0·09	0·74	0·69	0·06	0·07	0·53	0·02	0·02	0·65	0·14	0·21	0·24	0·18	
975°C, 200 MPa																
usc33	4	53·25	0·33	1·17	24·88	1·82	0·58	17·74	0·03	0·04	99·84	68·22	27·28	3·59	71·43	0·19
SD		1·08	0·06	0·41	0·15	0·07	0·20	0·51	0·01	0·01	0·99	0·10	0·57	0·16	0·46	
usc34	1	51·71	0·48	1·97	23·53	1·99	0·63	20·19	0·01	0·00	100·50	64·21	30·91	3·90	67·51	0·21
usc35	1	52·72	0·24	1·09	21·95	1·90	0·76	18·63	0·07	0·00	100·79	64·18	30·56	4·00	67·75	0·27
950°C, 200 MPa																
usc52	3	52·33	0·31	1·93	24·39	1·93	0·79	15·18	0·08	0·02	96·95	70·21	24·50	4·00	74·13	0·17
SD		0·91	0·03	0·12	0·30	0·19	0·16	0·68	0·02	0·03	0·91	0·20	0·79	0·45	0·66	
usc53	3	52·90	0·36	2·02	23·33	1·66	0·69	16·78	0·05	0·03	97·82	67·97	27·42	3·47	71·25	0·18
SD		0·07	0·08	0·36	0·15	0·28	0·08	0·41	0·06	0·01	0·08	0·57	0·52	0·59	0·51	
usc54	3	52·10	0·33	1·39	22·04	2·01	0·77	17·99	0·06	0·02	96·71	64·79	29·68	4·24	68·59	0·16
SD		0·14	0·06	0·17	0·18	0·30	0·04	0·29	0·06	0·04	0·50	0·33	0·38	0·59	0·29	
925°C, 200 MPa																
usc43	1	51·69	0·31	2·55	23·52	2·73	0·70	16·45	0·13	0·02	98·10	66·98	26·29	5·59	71·81	0·18
usc44	1	50·62	0·23	1·31	19·99	1·64	0·80	21·89	0·07	0·05	96·58	58·96	36·22	3·47	61·95	
900°C, 200 MPa																
usc59	1	47·39	0·20	1·55	17·97	2·10	0·93	24·04	0·18	0·04	94·40	53·64	40·27	4·51	57·11	
usc60	1	46·86	0·18	1·75	16·91	1·81	0·82	26·23	0·26	0·00		50·64	44·05	3·90	53·48	
1000°C, 400 MPa																
usc70	3	51·13	0·42	2·49	19·41	2·32	0·67	22·13	0·19	0·02	98·79	57·29	36·64	4·94	60·99	0·24
SD		0·71	0·09	0·59	0·65	0·38	0·08	0·77	0·11	0·02	0·46	0·89	0·67	0·91	0·68	
975°C, 400 MPa																
usc39	2	52·25	0·31	2·51	21·08	1·84	0·85	19·68	0·12	0·06	98·70	62·14	32·55	3·89	65·62	0·15
SD		0·32	0·00	0·46	0·21	0·41	0·21	0·36	0·08	0·04	0·61	0·93	0·43	0·86	0·64	
usc40	1	51·36	0·45	2·22	18·74	2·39	0·77	23·26	0·21	0·02	99·43	55·21	38·45	5·06	58·95	0·20
950°C, 400 MPa																
usc78	4	51·43	0·36	2·59	22·05	1·84	0·93	18·95	0·17	0·02	98·33	63·86	30·79	3·83	67·47	0·17
SD		0·57	0·03	0·80	0·59	0·25	0·16	0·41	0·14	0·04	1·37	0·52	0·25	0·56	0·25	
925°C, 400 MPa																
usc85	3	53·05	0·32	3·08	17·73	4·68	0·90	21·86	0·30	0·02	101·94	52·33	36·20	9·96	59·11	0·23
SD		1·02	0·11	1·22	1·35	0·23	0·11	1·64	0·27	0·02	1·08	0·81	0·32	0·79	0·48	
1000°C, 100 MPa																
usc73	5	52·98	0·43	1·88	25·84	2·02	0·90	15·89	0·06	0·03	100·04	70·37	24·28	3·95	74·34	0·24
SD		0·41	0·06	0·22	0·57	0·20	0·11	0·33	0·04	0·04	0·97	0·46	0·27	0·43	0·27	
usc74	2	52·04	0·38	3·58	22·41	2·53	0·89	17·31	0·54	0·06	99·73	65·06	28·19	5·28	69·77	0·25
SD		0·07	0·04	0·55	0·55	0·34	0·01	0·71	0·14	0·04	0·13	0·27	0·59	0·82	0·35	
975°C, 100 MPa																
usc58b	3	53·14	0·40	1·91	25·84	1·85	0·84	15·38	0·07	0·02	99·45	71·23	23·78	3·67	74·97	
SD		0·24	0·02	0·36	0·38	0·38	0·14	0·80	0·07	0·03	0·37	0·57	0·80	0·79	0·74	
usc59b		52·67	0·42	2·78	23·80	2·38	0·99	16·94	0·37	0·03	100·38	66·90	26·71	4·81	71·46	0·11
Reduced experiments																
1000°C, 200 MPa																
usc28	2	53·86	0·45	2·16	21·04	2·20	0·63	21·61	0·14	0·06	102·12	59·95	34·54	4·51	63·45	0·22
SD		1·38	0·05	0·08	1·00	0·13	0·12	0·97	0·20	0·08	0·42	0·27	0·05	0·47	0·07	
usc29	1	52·26	0·42	1·65	19·59	2·71	0·70	23·91	0·04	0·01	101·29	55·42	37·95	5·51	59·36	0·25
usc30	1	51·92	0·60	1·59	13·69	7·44	0·60	25·67	0·28	0·07	101·86	40·53	42·63	15·83	48·73	0·22
975°C, 200 MPa																
usc2	2	50·32	0·44	1·22	19·39	2·92	0·68	23·88	0·00	0·00	98·85	54·98	37·99	5·94	59·14	0·23
SD		0·12	0·00	0·00	0·01	0·26	0·07	0·29	0·00	0·00	0·49	0·62	0·05	0·46	0·30	
usc3	4	51·08	0·41	1·52	19·35	2·21	0·53	22·84	0·02	0·02	97·99	56·82	37·64	4·65	60·15	0·20
SD		0·29	0·07	0·16	0·26	0·25	0·09	0·11	0·04	0·04	0·51	0·38	0·38	0·47	0·26	
925°C, 200 MPa																
usc7	3	50·36	0·38	1·99	18·15	2·93	0·78	22·92	0·02	0·04	97·57	54·11	38·31	6·26	58·54	0·22
SD		0·61	0·03	0·39	0·35	0·68	0·08	0·44	0·04	0·04	0·71	1·66	0·23	1·38	0·89	
1000°C, 400 MPa																
usc25	3	52·46	0·51	1·83	20·60	2·73	0·68	21·00	0·06	0·01	99·89	59·32	33·91	5·66	63·64	0·23
SD		0·34	0·01	0·12	0·58	1·23	0·08	1·13	0·03	0·01	0·46	1·47	1·74	2·56	1·09	
975°C, 400 MPa																
usc12	2	50·88	0·32	5·06	17·81	2·78	0·42	18·96	0·54	0·05	96·83	58·04	34·65	6·53	62·62	0·26
SD		0·55	0·10	1·16	0·65	0·31	0·06	1·47	0·34	0·02	0·17	0·19	1·31	0·99	0·96	
usc13	1	51·01	0·28	0·94	19·21	2·00	0·57	23·52	0·00	0·04	97·56	56·22	38·62	4·21	59·28	0·29
usc14	1	50·47	0·40	1·80	16·82	4·05	0·65	22·18	0·07	0·06	96·50	51·69	38·23	8·94	57·49	
925°C, 400 MPa																
usc89	2	50·79	0·31	1·89	16·44	1·95	0·60	27·20	0·02	0·00	99·19	49·17	45·63	4·18	51·87	0·33
SD		0·03	0·06	0·27	0·15	0·00	0·20	1·06	0·01	0·00	0·78	0·49	0·92	0·08	0·75	

n, number of analysis; SD, standard deviation. FeO*, total iron reported as FeO. En, Fs and Wo were calculated as done by Morimoto (1989). Mg# = 100Mg/(Mg + Fe*). $K_d^{Fe^*–Mg}$ = (Fe*/Mg in clinopyroxene)/(Fe*/Mg in melt).

Table 6: Composition of experimental magnetites (wt %)

	n	SiO_2	TiO_2	Al_2O_3	MgO	CaO	MnO	FeO*	Na_2O	K_2O	Total	Mg#
Oxidized experiments												
1000°C, 200 MPa												
usc62	2	0·11	4·51	3·17	4·11	0·14	0·62	76·62	0·00	0·00	89·28	9·05
SD		0·05	0·19	0·10	0·03	0·01	0·12	0·71	0·00	0·00	0·86	
usc63	3	0·18	6·95	4·07	3·46	0·17	0·58	73·80	0·00	0·03	89·24	8·02
SD		0·06	0·12	0·02	0·10	0·06	0·08	0·69	0·00	0·03	1·01	
usc64	1	0·15	8·52	3·74	3·56	0·16	0·63	73·88	0·04	0·00	90·68	8·21
usc65	2	0·31	10·87	2·93	2·98	0·21	0·56	71·34	0·00	0·01	89·21	7·19
SD		0·16	0·03	0·06	0·14	0·02	0·13	0·79	0·00	0·02	0·91	
usc66	1	2·70	14·80	2·86	2·01	0·45	0·57	69·10	0·25	0·08	92·81	5·12
975°C, 200 MPa												
usc32	3	0·23	12·02	3·70	3·07	0·15	0·48	74·35	0·00	0·01	94·03	7·11
SD		0·17	0·15	0·13	0·20	0·11	0·07	0·55	0·01	0·01	0·58	
usc33	2	0·27	14·08	3·85	3·13	0·26	0·28	72·97	0·00	0·02	94·87	7·38
SD		0·14	0·06	0·11	0·04	0·17	0·07	0·02	0·00	0·03	0·43	
usc34	2	0·89	15·22	3·40	2·73	0·12	0·31	71·97	0·16	0·01	94·81	6·57
SD		0·35	0·68	0·22	0·06	0·06	0·08	1·04	0·02	0·01	0·01	
950°C, 200 MPa												
usc52	1	0·22	13·96	3·35	2·90	0·20	0·77	78·40	0·16	0·06	100·02	6·43
usc53	3	0·17	13·55	3·43	2·93	0·10	0·55	79·24	0·02	0·01	100·00	6·43
SD		0·04	0·22	0·03	0·06	0·08	0·40	1·19	0·00	0·02	0·97	
usc54	1	0·04	14·50	3·18	2·21	0·06	0·57	79·10	0·34	0·00	100·00	4·73
925°C, 200 MPa												
usc42	2	0·36	9·28	2·99	2·57	0·20	0·71	75·13	0·05	0·03	91·31	5·97
SD		0·00	0·17	0·29	0·05	0·06	0·05	0·11	0·07	0·04	0·16	
usc43	1	0·03	12·37	2·73	2·31	0·28	0·67	81·55	0·00	0·06	100·00	4·81
1000°C, 400 MPa												
usc70	2	0·27	16·75	3·74	2·53	0·23	0·38	66·19	0·04	0·03	90·16	6·62
SD		0·03	0·30	0·07	0·11	0·02	0·06	0·78	0·00	0·03	0·93	
950°C, 400 MPa												
usc77	2	0·15	5·72	3·13	3·52	0·11	0·58	77·03	0·00	0·04	90·29	7·82
SD		0·05	0·18	0·01	0·28	0·08	0·08	0·44	0·00	0·02	0·31	
usc78	2	0·36	9·17	3·18	2·39	0·19	0·65	75·49	0·00	0·06	91·49	5·55
SD		0·12	0·15	0·14	0·08	0·05	0·05	0·29	0·00	0·02	0·46	
usc79	1	0·39	10·39	2·64	1·87	0·27	0·32	74·50	0·07	0·05	90·51	4·46
usc80	3	0·26	10·65	2·60	1·93	0·20	0·49	76·10	0·00	0·01	92·23	4·49
SD		0·04	0·11	0·27	0·06	0·04	0·14	0·70	0·00	0·01	0·64	
925°C, 400 MPa												
usc82	3	0·25	9·08	3·28	2·01	0·16	0·59	76·69	0·01	0·00	92·06	4·47
SD		0·08	0·38	0·27	0·05	0·06	0·15	0·74	0·01	0·01	1·02	
usc83	3	0·24	9·96	3·39	1·69	0·10	0·61	77·19	0·03	0·07	93·28	3·75
SD		0·06	0·19	0·07	0·03	0·01	0·08	1·15	0·02	0·04	1·13	
usc84	5	0·26	11·55	3·31	1·75	0·19	0·59	76·84	0·00	0·03	94·52	3·91
SD		0·13	0·19	0·12	0·09	0·02	0·10	0·99	0·04	0·05	1·09	
usc85	3	0·35	12·26	3·02	1·56	0·17	0·46	77·27	0·02	0·00	95·12	3·47
SD		0·22	0·30	0·03	0·10	0·02	0·08	0·53	0·04	0·01	0·32	
1000°C, 100 MPa												
usc72	2	0·17	6·90	3·95	4·04	0·15	0·64	74·65	0·03	0·04	90·55	9·13
SD		0·00	0·27	0·02	0·10	0·06	0·14	1·08	0·04	0·03	1·36	
usc73	1	0·22	9·23	3·33	3·49	0·15	0·53	74·65	0·00	0·00	91·59	7·99
usc74	1	0·92	10·53	2·94	2·90	0·34	0·49	71·67	0·18	0·06	90·04	6·98
usc75	1	0·65	13·08	2·57	2·45	0·21	0·35	72·07	0·09	0·06	91·52	5·93
975°C, 100 MPa												
usc57b	2	0·16	6·84	3·49	4·16	0·15	0·66	76·32	0·00	0·06	91·82	9·19
SD		0·16	6·83	3·49	3·93	0·13	0·53	76·58	0·00	0·03	91·67	
usc58b	1	0·18	9·86	2·92	3·36	0·18	0·75	73·58	0·00	0·00	90·82	7·81
usc59b	1	0·17	11·07	2·63	3·04	0·14	0·62	73·04	0·00	0·05	90·76	7·18
usc60b	1	0·15	11·56	2·36	2·58	0·09	0·72	73·63	0·00	0·05	91·13	6·10
Reduced experiments												
1000°C, 200 MPa												
usc28	1	0·94	11·83	6·29	2·86	0·15	0·65	58·94	0·03	0·08	81·77	7·96
usc29	2	1·58	18·73	3·43	1·83	0·21	0·52	64·66	0·15	0·07	91·16	4·80
SD		0·16	2·45	0·98	0·34	0·03	0·11	2·62	0·06	0·02	3·95	
925°C, 200 MPa												
usc6	3	0·10	17·63	3·46	2·49	0·17	0·49	62·50	0·00	0·04	86·89	6·90
SD		0·08	0·45	0·17	0·15	0·06	0·09	0·68	0·00	0·01	0·81	
925°C, 400 MPa												
usc87	1	0·46	18·47	4·21	2·67	0·18	0·75	73·06	0·08	0·12	100·00	6·36

n, number of analyses; SD, standard deviation; FeO*, total iron reported as FeO. Mg# = 100(Mg/Mg + Fe*) in moles.

Table 7: Composition of experimental ilmenites (wt %)

	n	SiO_2	TiO_2	Al_2O_3	MgO	CaO	MnO	FeO*	Na_2O	K_2O	Total
Reduced experiments											
1000°C, 200 MPa											
usc28	3	0·14	49·84	0·29	3·65	0·25	0·48	45·04	0·04	0·05	99·79
SD		0·05	0·14	0·05	0·10	0·10	0·09	0·77	0·02	0·03	0·92
usc29	1	0·85	48·83	0·37	3·02	0·30	0·59	46·63	0·06	0·04	100·69
975°C, 200 MPa											
usc3	3	0·56	48·50	0·44	3·44	0·38	0·51	40·69	0·00	0·07	94·58
SD		0·43	0·35	0·18	0·08	0·02	0·13	0·83	0·00	0·02	0·67
975°C, 400 MPa											
usc12	1	0·24	50·11	0·23	4·46	0·46	0·61	39·80	0·00	0·12	96·02
925°C, 400 MPa											
usc87	2	0·34	46·40	0·24	3·19	0·27	0·57	41·94	0·16	0·00	93·12
SD		0·12	0·02	0·06	0·13	0·02	0·27	0·02	0·08	0·00	0·43
usc88	1	0·20	46·74	0·20	2·68	0·29	0·73	42·86	0·03	0·04	93·77
usc89	1	0·94	47·63	0·65	2·75	0·39	0·81	42·72	0·08	0·06	96·03

n, number of analyses; SD, standard deviation. FeO*, total iron reported as FeO.

Table 8: Composition of experimental amphiboles (after Leake *et al.*, 1997)

	usc42(3)	SD	usc82(3)	SD	usc83(5)	SD	usc84(4)	SD	usc6(4)	SD	usc87(2)	SD	usc88(5)	SD	usc89(3)	SD
SiO_2	41·45	0·28	43·21	0·36	43·12	0·37	44·31	0·52	41·73	0·55	42·42	0·92	41·06	0·40	41·66	0·10
TiO_2	3·01	0·04	2·39	0·19	2·68	0·16	2·97	0·22	3·28	0·13	2·55	0·46	3·16	0·24	3·44	0·19
Al_2O_3	10·99	0·56	11·72	0·39	11·32	0·55	10·31	0·48	10·75	0·36	10·50	0·17	11·73	0·14	10·83	0·28
FeO*	11·34	0·14	12·89	1·22	14·44	0·43	14·80	0·61	13·24	0·56	15·51	0·47	16·76	0·52	17·89	0·24
MnO	0·28	0·01	0·35	0·10	0·24	0·13	0·32	0·11	0·28	0·06	0·21	0·11	0·25	0·06	0·22	0·11
MgO	14·47	0·23	13·67	0·88	12·08	0·16	12·68	0·53	12·74	0·36	11·47	0·18	9·91	0·45	10·12	0·35
CaO	11·21	0·20	11·17	0·06	11·39	0·43	10·25	0·20	10·61	0·19	10·83	0·01	10·83	0·24	9·99	0·14
Na_2O	2·12	0·05	2·35	0·04	2·40	0·11	2·29	0·08	2·12	0·07	2·42	0·11	2·36	0·07	2·35	0·12
K_2O	1·09	0·44	0·46	0·04	0·46	0·06	0·39	0·03	0·35	0·03	0·32	0·02	0·49	0·05	0·46	0·04
Sum	95·97	0·19	98·20	1·15	98·13	0·42	98·31	0·79	95·11	0·28	96·25	0·20	96·59	0·33	97·06	0·52
atoms per formulae																
Si	6·13		6·22		6·31		6·38		6·22		6·34		6·19		6·21	
Ti	0·33		0·26		0·30		0·32		0·37		0·29		0·36		0·39	
Al_{tot}	1·91		1·99		1·95		1·75		1·89		1·85		2·08		1·90	
Fe^{3+}	0·80		0·86		0·48		0·96		0·86		0·66		0·55		0·95	
Fe^{2+}	0·60		0·69		1·28		0·82		0·79		1·28		1·57		1·28	
Mn	0·04		0·04		0·03		0·04		0·04		0·03		0·03		0·03	
Mg	3·19		2·94		2·64		2·72		2·83		2·56		2·23		2·25	
Ca	1·78		1·72		1·79		1·58		1·69		1·73		1·75		1·60	
Na	0·61		0·66		0·68		0·64		0·61		0·70		0·69		0·68	
K	0·21		0·09		0·09		0·07		0·07		0·06		0·09		0·09	
AlIV	1·87		1·78		1·69		1·62		1·78		1·66		1·81		1·79	
A sites	0·59		0·46		0·55		0·29		0·38		0·50		0·53		0·36	
Mg#	0·69		0·65		0·60		0·60		0·63		0·57		0·41		0·51	

Numbers in parentheses indicate the number of analyses. SD, standard deviation. FeO*, total iron reported as FeO. Mg# = MgO/(MgO + FeO*) in wt %. A sites = (Na + K).

at 200 MPa and with 4–5 wt % H_2O_{melt} successfully reproduce the Pl/Opx ratio (12) and crystal content (28 wt %) of the natural andesite, whereas those at 400 MPa would require crystallinities of 50 wt % to achieve the same ratio (Fig. 9c).

Glasses obtained at 200 MPa and NNO + 1·5 also successfully reproduce the composition of the residual melt of the andesite (Table 1; Fig. 8). Although there are not large differences between most major oxides (i.e. SiO_2, Al_2O_3, CaO, Na_2O, K_2O) of the glasses obtained at either 200 or 400 MPa and 975–1000°C, charges at 400 MPa generally have glasses with lower TiO_2 contents (even considering analytical uncertainties), and higher FeO*/MgO ratios, than those at 200 MPa (Fig. 8).

The comparison between natural and experimental phase relationships and mineral compositions therefore constrains the pre-eruptive P–T–H_2O_{melt}–fO_2 conditions for the Upper Scoriae 1 andesite to be 200 MPa, 975–1000°C, 5 ± 0·5 wt % H_2O_{melt} and $fO_2 \sim$ NNO + 1·5 (Table 2; Fig. 3). Such conditions are similar to previous estimates obtained for andesitic magmas at Santorini (Gardner *et al.*, 1996; Michaud *et al.*, 2000). We note that coexisting Fe–Ti oxides in evolved ($T < 900$°C) Santorini magmas yield fO_2 between QFM − 0·5 and NNO + 0·5 (Nichols, 1971*a*; Cottrell *et al.*, 1999; Cadoux *et al.*, 2014;

Table 9: Composition of experimental glasses (wt %)

	n	SiO_2	TiO_2	Al_2O_3	FeO*	MnO	MgO	CaO	Na_2O	K_2O	P_2O_5	Total	Sum	FeO*/MgO
Oxidized experiments														
1000° C, 200 MPa														
usc62	11	60·87	1·15	16·41	5·85	0·20	2·77	6·55	4·45	1·38	0·37	100	92·4	2·1
SD		0·13	0·08	0·14	0·06	0·21	0·08	0·21	0·14	0·05	0·07		0·6	
usc63	3	62·03	1·12	17·15	5·59	0·08	2·28	5·79	4·50	1·47	0·00	100	92·7	2·4
SD		0·18	0·03	0·32	0·23	0·13	0·06	0·17	0·15	0·08	0·00		0·7	
usc65	4	65·97	0·94	15·36	5·08	0·19	1·27	3·74	4·72	2·36	0·38	100	95·4	4·0
SD		0·44	0·07	0·79	0·40	0·14	0·07	0·34	0·06	0·07	0·11		0·5	
usc66	3	70·21	0·85	13·38	4·62	0·09	0·63	2·30	4·24	3·46	0·22	100	96·4	7·3
SD		0·57	0·11	0·20	0·11	0·10	0·07	0·14	0·12	0·06	0·08		0·8	
975° C, 200 MPa														
usc32	5	60·18	0·98	16·75	7·58	0·28	2·20	5·74	4·46	1·52	0·32	100	94·6	3·4
SD		0·59	0·15	0·33	0·21	0·15	0·06	0·12	0·27	0·03	0·02		0·6	
usc33	5	60·35	1·09	16·39	7·72	0·22	2·05	5·56	4·63	1·60	0·39	100	95·5	3·8
SD		0·30	0·07	0·13	0·16	0·12	0·05	0·19	0·11	0·13	0·07		0·3	
usc34	2	62·93	1·07	15·65	6·70	0·24	1·66	4·57	4·87	1·91	0·40	100	96·3	4·0
SD		0·14	0·04	0·08	0·22	0·02	0·00	0·12	0·03	0·00	0·11		0·6	
usc35	4	65·30	1·00	14·74	6·21	0·15	1·19	3·73	4·73	2·48	0·47	100	97·7	5·2
SD		0·22	0·05	0·16	0·20	0·11	0·04	0·16	0·19	0·05	0·05		0·5	
usc36	2	67·48	0·89	13·49	5·71	0·15	0·70	3·14	4·52	3·31	0·60	100	97·7	8·2
SD		0·56	0·04	0·01	0·01	0·02	0·03	0·35	0·04	0·14	0·36		0·4	
950° C, 200 MPa														
usc52	3	69·11	0·62	15·42	3·36	0·07	0·78	3·04	4·76	2·56	0·28	100	93·1	4·3
SD		0·97	0·11	0·38	0·01	0·04	0·04	0·46	0·21	0·25	0·10		0·7	
usc53	5	68·99	0·65	14·77	3·71	0·19	0·94	2·87	5·09	2·57	0·22	100	95·5	3·9
SD		0·15	0·07	0·04	0·37	0·08	0·03	0·13	0·12	0·04	0·05		0·4	
usc54	3	71·37	0·54	14·25	3·37	0·12	0·64	2·16	4·41	2·92	0·21	100	97·4	5·3
SD		0·64	0·04	0·44	0·24	0·03	0·10	0·24	0·10	0·15	0·11		1·0	
925° C, 200 MPa														
usc42	5	66·54	0·63	16·41	3·88	0·07	1·09	4·40	5·08	1·70	0·19	100	94·8	3·6
SD		0·33	0·06	0·15	0·16	0·07	0·08	0·04	0·41	0·11	0·05		0·6	
usc43	3	70·91	0·48	14·27	2·87	0·07	0·74	2·55	5·39	2·58	0·14	100	96·2	3·9
SD		0·25	0·05	0·31	0·24	0·05	0·05	0·08	0·15	0·09	0·07		0·4	
1000° C, 400 MPa														
usc67	10	58·45	1·36	16·29	8·77	0·20	2·90	6·37	3·82	1·51	0·35	100	89·7	3·0
SD		0·39	0·08	0·23	0·28	0·06	0·21	0·36	0·18	0·29	0·06		0·6	
usc68	14	58·56	1·32	16·37	8·39	0·15	2·58	6·18	4·67	1·44	0·34	100	94·9	3·3
SD		0·43	0·08	0·52	0·30	0·10	0·40	0·64	0·25	0·11	0·09		0·8	
usc69	10	58·98	1·31	16·36	8·14	0·15	2·58	6·15	4·57	1·44	0·32	100	94·5	3·2
SD		0·70	0·10	0·57	0·37	0·09	0·52	0·68	0·25	0·10	0·05		0·6	
usc70	3	62·20	1·30	15·38	8·09	0·09	1·72	4·69	4·09	2·04	0·40	100	94·6	4·7
SD		0·43	0·09	0·05	0·59	0·12	0·03	0·08	0·34	0·08	0·04		0·4	
usc71	4	65·21	1·10	13·94	7·03	0·23	0·90	3·78	4·30	3·04	0·47	100	96·2	7·8
SD		0·84	0·05	0·18	0·56	0·09	0·01	0·08	0·21	0·08	0·11		0·3	
975° C, 400 MPa														
usc37	5	59·69	1·21	15·83	8·11	0·24	2·54	6·32	4·40	1·33	0·32	100	91·4	3·2
SD		0·47	0·11	0·21	0·18	0·07	0·11	0·09	0·46	0·11	0·09		0·7	
usc38	5	60·64	1·02	17·49	7·26	0·16	1·80	5·26	4·53	1·51	0·34	100	95·3	4·0
SD		0·38	0·07	0·16	0·43	0·05	0·11	0·17	0·17	0·08	0·07		0·5	
usc39	3	62·08	0·78	17·37	6·31	0·37	0·99	5·10	4·78	1·86	0·37	100	95·7	6·4
SD		0·34	0·09	1·02	0·85	0·10	0·09	0·45	0·29	0·27	0·06		0·5	
usc40	4	66·14	0·84	14·43	6·41	0·12	1·01	3·50	4·62	2·42	0·53	100	96·1	6·4
SD		0·11	0·08	0·17	0·17	0·01	0·02	0·02	0·27	0·02	0·02		0·5	
950° C, 400 MPa														
usc77	3	62·76	1·11	17·26	4·69	0·12	2·17	5·72	4·37	1·44	0·37	100	91·9	2·2
SD		0·53	0·04	0·22	0·44	0·10	0·07	0·20	0·20	0·11	0·07		0·4	
usc78	3	70·59	0·48	14·48	3·85	0·14	0·78	3·00	4·06	2·45	0·18	100	97·0	5·0
SD		0·33	0·11	0·43	0·52	0·05	0·10	0·02	0·10	0·08	0·11		0·8	
925° C, 400 MPa														
usc82	10	64·62	0·61	17·25	4·26	0·17	1·17	5·57	4·55	1·66	0·15	100	91·7	3·7
SD		0·76	0·13	0·32	0·36	0·07	0·06	0·07	0·82	0·07	0·11		0·7	
usc83	1	65·23	0·78	16·93	5·12	0·22	0·66	4·43	4·78	1·67	0·17	100	93·9	7·8
usc84	9	68·32	0·54	15·38	3·85	0·11	0·85	3·52	5·01	2·27	0·17	100	94·0	4·6
SD		0·42	0·05	0·24	0·46	0·09	0·10	0·12	0·08	0·12	0·15		0·7	
usc85	9	70·74	0·39	14·72	3·30	0·08	0·59	2·68	4·42	2·97	0·10	100	94·3	5·6
SD		0·29	0·09	0·22	0·11	0·08	0·04	0·09	0·37	0·07	0·08		0·4	
1000° C, 100 MPa														
usc72	4	63·30	1·08	16·06	5·16	0·23	1·87	5·65	4·70	1·69	0·25	100	95·9	2·8
SD		0·33	0·09	0·14	0·11	0·08	0·03	0·40	0·23	0·05	0·03		0·7	
usc73	4	65·28	0·94	15·30	4·92	0·20	1·51	4·45	5·08	1·92	0·41	100	96·3	3·3
SD		0·31	0·04	0·20	0·09	0·07	0·09	0·20	0·25	0·15	0·09		1·0	
usc74	2	68·94	0·81	13·96	4·16	0·10	1·32	3·29	4·77	2·26	0·40	100	97·8	3·1
SD		0·65	0·03	0·53	0·24	0·06	0·03	0·26	0·31	0·06	0·15		0·5	
usc75	3	71·91	0·48	13·27	2·87	0·07	0·74	2·55	5·39	2·58	0·14	100	97·7	3·9

(continued)

Table 9. Continued

	n	SiO_2	TiO_2	Al_2O_3	FeO*	MnO	MgO	CaO	Na_2O	K_2O	P_2O_5	Total	Sum	FeO*/MgO
SD		0·33	0·09	0·61	0·47	0·01	0·01	0·22	0·09	0·14	0·01		0·3	
usc76														
975°C, 100 MPa														
usc57b	2	64·10	1·05	16·22	4·67	0·28	2·09	5·02	4·56	1·69	0·32	100	95·1	2·2
SD		0·34	0·06	0·25	0·32	0·14	0·09	0·03	0·41	0·04	0·04		0·2	
usc59b	1	71·31	0·75	13·28	3·63	0·20	0·77	2·56	4·20	2·96	0·34	100	95·8	4·7
Reduced experiments														
1000°C, 200 MPa														
usc27	10	59·19	1·30	16·23	8·23	0·21	2·42	6·41	4·29	1·52	0·20	100	92·5	3·4
SD		0·43	0·17	0·09	0·42	0·09	0·05	0·11	0·07	0·11	0·06		0·5	
usc28	4	61·91	0·94	16·10	7·58	0·10	1·59	5·06	4·72	1·83	0·16	100	94·6	4·8
SD		0·45	0·11	0·11	0·27	0·08	0·05	0·11	0·20	0·10	0·12		0·9	
usc29	1	64·44	0·83	14·72	6·90	0·27	1·43	4·21	4·83	2·09	0·29	100	94·9	4·8
usc30	4	66·60	0·74	15·29	5·48	0·14	0·65	2·90	5·14	2·84	0·21	100	95·9	8·5
SD		0·45	0·16	0·05	0·16	0·01	0·04	0·04	0·23	0·05	0·03		1·0	
975°C, 200 MPa														
usc1	8	58·97	1·30	15·58	8·76	0·23	2·78	6·42	4·34	1·47	0·17	100	93·3	3·2
SD		0·65	0·12	0·22	0·16	0·10	0·04	0·12	0·40	0·07	0·10		0·6	
usc2	2	62·41	1·08	15·65	7·72	0·20	1·44	4·66	4·60	2·03	0·20	100	96·6	5·4
SD		0·93	0·02	0·52	0·17	0·07	0·00	0·13	0·76	0·24	0·01		0·1	
usc3	1	62·56	1·07	15·57	7·95	0·03	1·36	4·88	4·50	1·96	0·10	100	96·9	5·8
usc4	5	65·34	0·97	14·43	6·76	0·23	1·10	3·73	4·64	2·50	0·28	100	98·3	6·1
SD		0·29	0·15	0·17	0·34	0·13	0·03	0·06	0·23	0·15	0·11		0·3	
usc5	1	69·85	0·96	13·42	4·67	0·17	0·70	2·78	4·07	3·32	0·06	100	98·5	6·7
925°C, 200 MPa														
usc6	3	62·52	0·87	16·72	6·86	0·05	1·57	5·45	4·49	1·48	0·00	100	92·3	4·4
SD		0·57	0·01	0·12	0·21	0·05	0·04	0·02	0·33	0·05	0·00			
usc7	1	64·38	0·74	16·22	5·94	0·31	1·03	3·99	4·94	2·25	0·21	100	95·6	5·8
usc8	2	67·95	0·75	14·78	4·77	0·05	0·66	3·01	4·90	2·90	0·24	100	95·4	7·2
SD		0·21	0·05	0·01	0·33	0·04	0·02	0·11	0·11	0·14	0·00		0·5	
1000°C, 400 MPa														
usc22	1	58·82	1·35	16·13	8·77	0·14	2·54	6·43	4·19	1·40	0·25	100	92·8	3·5
usc23	1	59·19	1·30	16·23	8·23	0·21	2·42	6·41	4·29	1·52	0·20	100	95·7	3·4
usc25	3	61·31	1·24	16·32	7·65	0·18	1·72	4·88	4·59	1·85	0·24	100	97·6	4·4
SD		0·26	0·10	0·37	0·28	0·00	0·06	0·10	0·04	0·03	0·02		0·4	
usc26	2	64·85	1·15	15·04	6·02	0·09	1·18	3·89	4·97	2·45	0·36	100	97·9	5·1
SD		0·08	0·13	0·03	0·04	0·04	0·06	0·03	0·05	0·02	0·01		0·3	
975°C, 400 MPa														
usc11	4	59·00	1·33	15·83	8·80	0·12	2·65	6·58	4·08	1·27	0·35	100	91·5	3·3
SD		0·53	0·10	0·14	0·11	0·08	0·13	0·40	0·38	0·02	0·08		0·7	
usc12	3	61·56	1·10	16·06	7·56	0·01	1·82	5·14	4·80	1·61	0·35	100	93·9	4·2
SD		0·19	0·01	0·06	0·06	0·01	0·08	0·08	0·19	0·08	0·11		0·1	
usc13	3	62·70	1·10	15·42	7·19	0·03	1·70	5·03	4·67	1·81	0·35	100	94·6	4·2
SD		0·61	0·07	0·12	0·28	0·05	0·13	0·78	0·37	0·16	0·09		0·3	
925°C, 400 MPa														
usc87	10	61·81	0·84	16·53	6·74	0·15	1·63	5·70	4·87	1·55	0·18	100	90·1	4·1
SD		0·51	0·09	0·13	0·22	0·10	0·03	0·11	0·36	0·06	0·12		0·7	
usc88	3	62·88	0·73	17·03	5·50	0·19	1·14	5·07	5·50	1·74	0·23	100	92·7	4·8
SD		0·57	0·03	0·09	0·18	0·06	0·03	0·02	0·37	0·06	0·02		0·5	
usc89	9	65·44	0·55	15·72	5·36	0·13	0·93	3·84	5·66	2·13	0·24	100	94·0	5·8
SD		0·33	0·09	0·14	0·25	0·08	0·05	0·08	0·36	0·11	0·10		0·5	
usc90	3	69·07	0·60	15·47	3·69	0·05	0·73	2·85	4·60	2·81	0·12	100	94·1	5·0
SD		0·08	0·06	0·15	0·29	0·08	0·02	0·09	0·11	0·13	0·05		0·5	

All analyses are normalized to 100% anhydrous. Original totals are reported (Sum). *n*, number of analyses; SD, standard deviation. FeO*, total iron reported as FeO.

Druitt, 2014); however, there are no oxide-based estimates of fO_2 for intermediate or mafic magmas. Our data show that the USC-1 andesite fractionated under conditions more oxidizing than NNO, and perhaps as high as NNO + 1·5.

Evidence for magma reheating prior to eruption

The textural and compositional variations observed in crystals (xenocrysts and phenocrysts) from the studied andesitic sample can provide information concerning the dynamics operating within the magma reservoir. We now use these variations, along with the results of our experiments, and with data from previous experiments and from the literature, to provide insights concerning the evolution of the USC-1 magma and the dynamics of the reservoir prior to the eruption.

As previously pointed out, during the USC-1 eruption two different magmas were erupted: the volumetrically dominant (≫99%) andesite and a volumetrically subordinate dacite (62·0–63·2 wt % SiO_2), which appears as scattered and very rare pumices within the USC-1 fall-out deposit (Druitt *et al.*, 1999). Unfortunately, there are

no petrological data on the dacitic pumice. However, Andújar *et al.* (2015) reported the occurrence of felsic minerals dispersed within the USC-1 andesite; in particular, the presence of low-Mg orthopyroxene xenocrysts ($En_{55}Fs_{40}Wo_4$, Mg#58), Mg-poor augite ($En_{38}Fs_{23}Wo_{39}$, Mg#63) and low-An plagioclase ($An_{45–50}$), whose compositions mimic those of Santorini dacites (see above). Thus, as for the andesite, this information can be used to shed light on the storage conditions of the USC-1 dacite.

Phenocrysts of inferred dacitic provenance [see Andújar *et al.* (2015) for further details] provide the following constraints. The $En_{55}Fs_{40}Wo_4$, Mg#58 Opx is reproduced at 900°C, 200 MPa with 5–6 wt % H_2O_{melt} (Fig. 7; Table 5). Such water contents do also reproduce the Mg-poor augite ($En_{38}Fs_{23}Wo_{39}$, Mg#63) and the $An_{45–50}$ from the dacite at the same pressure and fO_2, although at somewhat higher temperatures (925–950°C; Figs 4 and 5). In contrast, pressures as high as 400 MPa, NNO + 1·5 or an fO_2 at QFM can be both ruled out because at such conditions Pl is either less (at 400 MPa) or more (at QFM) calcic compared with Pl from the dacite (Fig. 4). Thus, we conclude that the dacitic magma was probably stored at 200 MPa, at temperatures between 900 and 950 °C with 5–6 H_2O_{melt} wt %, in broad agreement with previous T–H_2O wt % constraints for dacitic magmas at Santorini (Druitt *et al.*, 1999; Fabbro *et al.*, 2013; Cadoux *et al.*, 2014). Using these values and the $An_{45–50}$ Pl composition as inputs in equations (1)–(3) yields crystal contents for the USC-1 dacite between 50 and 66 (± 1·4) wt %, Wo contents in clinopyroxene of 40 ± 1·2 mol %, and Mg# in magnetite of 6 ± 0·6 mol %, in good agreement with the compositions of the main phenocrysts of the USC-1 dacite and those of Santorini (this work; Druitt *et al.*, 1999).

The presence of resorbed textures on the $En_{55}Fs_{40}Wo_4$, Mg#58 Opx of the USC-1 andesite and the fact that they are commonly mantled by a more Mg-rich composition ($En_{65}Fs_{29}Wo_4$, Mg#68) both suggest that the dacite experienced an episode of magma mixing with a hotter and more mafic magma; in such a scenario the USC-1 andesite would be responsible for the Mg-rich mantle (or higher En molar per cent) and crystal resorption of the dacitic Opx (Andújar *et al.*, 2015). The fact that the andesitic Opx ($En_{65}Fs_{29}Wo_4$, Mg#68) mantling dacitic Opx is in turn overgrown by augite ($En_{42–44}Fs_{19–21}Wo_{37}$, Mg#67–70) from the andesite (see Andújar *et al.*, 2015, fig. 6), and the lack of reaction rims between them, suggests that these phases crystallized together, the sequence of Cpx $En_{44}Fs_{19}Wo_{37}$Mg#70 → $En_{42}Fs_{21}Wo_{37}$Mg#67 thus representing a phase of cooling of the system from 1000°C to 975°C after andesite intrusion into the dacitic magma body. We infer that the main andesite and subordinate dacite magmas were ponding at the same depth (200 MPa), this being the intrusion level of the USC-1 andesite into the partially crystallized dacitic magma body (50–66 wt % crystals) that then formed a compositionally and thermally zoned, highly crystallized magma reservoir or mush. It is worth noting that these conditions differ from those of andesite production, which has been inferred to occur at 400 MPa, 1000°C and $fO_2 \sim$ QFM, subsequent to basalt crystallization (Andújar *et al.*, 2015). The latter observation suggests that a decrease in pressure accompanied by an increase in oxidation state may have occurred prior to and during the intrusion of the natural andesite. The oxidation of the magma could be due to the assimilation of shallower limestone or marble wall-rocks (Nichols, 1971*b*; Zellmer *et al.*, 2000; Iacono-Marziano *et al.*, 2008; Spandler *et al.*, 2012) and/or to volatile exsolution during decompression (Burgisser & Scaillet, 2007).

Finally, the presence of xenocrystic phases such as olivine, An-rich Pl and high-Mg diopside, some of which partly re-equilibrated with the andesitic magma (as indicated by their compositional zoning), bears evidence of an intrusion of basaltic–basaltic andesitic magma prior to the eruption, which may have provided the trigger mechanism of the USC-1 eruption (see Andújar *et al.*, 2015).

Based on the above, the following sequence of events for the late magmatic evolution of the USC-1 magma reservoir can be proposed. The andesitic magma that was generated from basalt crystallization at 12–15 km depth rose to shallower levels and intruded a partially crystallized dacitic body that was at 950–925°C and 8 km depth. This increased the temperature of the more evolved magma and generated the resorption textures of dacitic Opx entrained into the andesite. The subsequent cooling of the system from 1000 to 975°C led to the crystallization of the andesite magma, which generated the Mg-rich rims observed on Opx and the main phase assemblage and composition of the andesite. However, the cooling process did not trigger the eruption of the system by itself. The arrival of a new hotter basaltic–basaltic andesitic magma into the system may have triggered the eruption sometime later, as evidenced by the presence of mafic xenocrysts (olivine, An-rich Pl, and high-Mg diopside; see above; Andújar *et al.*, 2015).

The above model for the USC-1 magma reservoir is consistent with an open system characterized by abrupt changes in temperature and composition, as a result of magma mixing–mingling processes at Santorini, which have been recorded in the eruptive products of the island (Nichols, 1971*a*; Huijsmans *et al.*, 1988; Druitt *et al.*, 1999; Zellmer *et al.*, 2000; Fabbro *et al.*, 2013).

Conditions for melt evolution at Santorini: role of temperature and fO_2

Major explosive eruptions at Santorini over the last 550 kyr have been dominated by the emission of intermediate (andesite–dacite; Cape Therma 1, Cape Thera, Upper Scoriae 1, Upper Scoriae 2; Druitt *et al.*, 1999) and silicic magmas (dacite–rhyodacite; Cape Therma 2, Lower Pumice 1, Lower Pumice 2, Cape Riva, Minoan). Despite their mineralogical similarities, the two groups

exhibit systematic compositional differences (Druitt *et al.*, 1999). In particular, andesite–dacite magmas of the intermediate-dominated eruptions have higher FeO*/MgO ratios and TiO_2 contents compared with their silicic counterparts, and most have tholeiitic affinities (Fig. 10a–d). In contrast, dacites (and minor andesitic components) from the silicic-dominated eruptions fall in the calc-alkaline field (Fig. 10a–d), but rhyodacites (>68 wt % SiO_2) exhibit greater variability in their FeO*/MgO ratios and straddle the calc-alkaline and tholeiitic fields (Fig. 10a and b). Such differences probably reflect temporal changes in the generation, evolution and/or storage conditions of the magmas at Santorini (Nichols, 1971*a*; Huijsman *et al.*, 1988; Druitt *et al.*, 1999; Mortazavi & Sparks, 2004).

Experimental liquids produced by the crystallization of the USC-1 andesite reproduce the liquid line of descent defined by Santorini magmas (Fig. 10). This confirms the success of our experimental approach and gives support to models in which crystal fractionation is the main process controlling magma evolution at Santorini, even if the presence of mafic material dispersed within the main volume of the deposits reflects a common and recurrent process of injection of less evolved magmas into a more evolved magma. However, as previously stated, the petrology and geochemistry of the erupted products at Santorini show that mixing plays a subordinate role in magma evolution (Nichols, 1971*a*; Huijsmanns *et al.*, 1988; Druitt *et al.*, 1999; Michaud *et al.*, 2000; Zellmer *et al.*, 2000), yet it possibly acts as an eruption trigger. Protracted chemical mixing as a main controlling factor of magma evolution requires specific conditions to occur (Laumonier *et al.*, 2014), which are often met at many calc-alkaline volcanoes, but apparently less so at Santorini. Experimental liquids define different compositional lineages depending on P–T–fO_2–H_2O_{melt} (Fig. 10). On a diagram of TiO_2 versus SiO_2, melts produced at 1000–975°C fall in the intermediate-dominated (andesite–dacite) magma field whereas those at 950–900°C fall within the silicic-dominated region, regardless of the prevailing fO_2 and pressure (Fig. 10c and d). This relationship provides first-order constraints on the temperature of the erupted magmas, andesites and dacites being characterized by higher temperatures (1000–975°C) than dacites and rhyodacites (950–850°C). The experimental results also shed light on the difference in the glass TiO_2 content between these two groups. In NNO + 1·5 experiments the relationship of glass TiO_2 content with temperature is strongly correlated with the onset of ilmenite crystallization at $T < 965$°C and the increasing modal proportion of ilmenite and magnetite with magma evolution (Fig. 3; Table 2). Charges annealed at 1000–975°C are characterized by the highest glass TiO_2 content and the absence of ilmenite in the crystallizing assemblage, whereas in those at $T < 950$°C ilmenite crystallizes together with significant amounts of magnetite, leading to an overall decrease in the TiO_2 content of the melt (Table 2; Figs 8 and 10). This observation is consistent with previous temperature constraints (1080–960°C; Michaud *et al.*, 2000) and with the petrology of recent eruptive products at Santorini in which andesites are characterized by the lack of ilmenite in their mineral assemblages (i.e. USC-1, USC-2, Cape Therma 1–3, Middle Pumice andesite, recent Kameni products; Nichols, 1971*a*; Barton & Huijsmann, 1986; Druitt *et al.*, 1999; Michaud *et al.*, 2000; this work). In contrast, the products of dominantly silicic eruptions have lower TiO_2 contents, contain ilmenite and have pre-eruptive temperatures of ≤900°C (Gardner *et al.*, 1996; Cottrell *et al.*, 1999; Gertisser *et al.*, 2009; Cadoux *et al.*, 2014). This is in agreement with our experimental results. These observations imply that an $fO_2 \sim$ NNO + 1·5 to NNO + 0·5 (average NNO + 1 ± 0·5; Tables 2 and 9) prevailed for all of the Santorini evolved magmas; this is again consistent with our previous fO_2 estimate for the USC-1 magma.

The above does not rule out the possibility that this was not the case for the more evolved compositions (dacites–rhyodacites from the silicic group) because (1) these rocks contain ilmenite (see above) and (2) liquids of the QFM experiments show the same relationship between temperature and melt TiO_2 content (Fig. 10c and d). Ilmenite also crystallizes over the range of explored temperatures (1000–925°C) at QFM, but the modal abundances of magnetite and/or ilmenite are somewhat lower compared with the NNO + 1·5 experiments (Table 2). We therefore use the plot FeO*/MgO vs SiO_2 to better constrain the fO_2 prevailing in the system (Fig. 10a and b). This plot shows that, except for a single run (925°C, 400 MPa), QFM glasses plot outside the field defined by Santorini magmas. In contrast, a large number of NNO + 1·5 to NNO + 0·5 experimental glasses do fall within the Santorini field. This shows conclusively that differentiation of an andesitic magma under reducing conditions (≤QFM) does not produce dacitic–rhyodacitic liquids that follow the lineage defined by Santorini melts. Thus, more oxidizing conditions (NNO + 0·5 to NNO + 1·5; Table 2) are required to explain the FeO*/MgO ratio of Santorini magmas.

Conditions required for the generation of tholeiitic or calc-alkaline dacites–rhyodacites at Santorini

Our experimental results can shed light on the generation conditions and mechanisms controlling the calc-alkaline versus tholeiitic affinities of magmas at Santorini. Younger (<530 ka) andesitic, dacitic and rhyodacitic magmas at Santorini have tholeiitic to weakly calc-alkaline affinities depending on their FeO*/MgO ratios (Fig. 10a and b; Druitt *et al.*, 1999). The tholeiitic character has been attributed to the differentiation of a basaltic magma under reduced conditions where magnetite crystallization is either suppressed or occurs in low modal proportions, allowing the Fe enrichment characteristic of tholeiitic series magmas (Sisson & Grove, 1993; Druitt *et al.*, 1999; Andújar *et al.*, 2015). In

contrast, the calc-alkaline trend is acquired when the magma evolves under oxidizing conditions (>NNO), which promote a massive precipitation of magnetite. Additionally, it may also arise by mixing an evolved magma (dacite–rhyodacite) with a more mafic melt (basalt, basaltic andesite), resulting in a decrease in the Fe content of the mixed magmas and low FeO*/MgO ratios (Sisson & Grove, 1993; Druitt *et al.*, 1999; Fabbro *et al.*, 2013). As detailed below, our experimental results provide an alternative mechanism whereby the tholeiitic or calc-alkaline affinities reflect the pressure of magma provenance.

Our data show that the crystallization of USC-1 andesite at NNO + 1 ± 0·5 generates residual melts that have different FeO*/MgO ratios depending on the prevailing temperature and/or pressure (Fig. 10). At 1000–975 °C, glasses produced at 100 MPa all lie within (or in one case on the boundary of) the calc-alkaline field, whereas all 400 MPa glasses lie in the tholeiitic field; glasses at 200 MPa straddle the two fields. At 950–925°C, both the 200 and 400 MPa data straddle the two fields, but more of the 200 MPa melts are calc-alkaline and more of the 400 MPa melts are tholeittic. Hence, it is apparent that the higher the pressure, the more tholeiitic the liquid line of descent.

We have therefore used the pressure–temperature dependence of the FeO*/MgO of the melt at NNO + 1 ± 0·5 to define broad domains corresponding to different pressure and temperature intervals (1000–975°C, red dashed lines or 950–850°C, blue dotted lines, Fig. 11). It is worth noting that the maximum SiO_2 content reached by our experimental melts does not exceed 72 wt % whereas the residual melts of major rhyodacitic eruptions exceed this SiO_2 content (e.g. Druitt *et al.* 1999). Thus we used the data of Cadoux *et al.* (2014), who performed experiments on four major rhyodacitic eruptions and at similar conditions (850°C, 100–200 MPa, fO_2 ~ NNO + 1), to define the shape of the curves for SiO_2 >72 wt %. Figure 11a (and Fig. 10a and b) clearly shows that at temperatures of 1000–975°C, shallow conditions (100 MPa) are required to generate calc-alkaline dacitic–rhyodacitic melts whereas tholeiitic equivalents require pressures between 200 and 400 MPa (Figs 10b and 11a). At 950–850°C and for SiO_2 contents up to 72 wt %, the pressure needed to generate dacites–rhyodacites with tholeiitic affinities is 400 MPa whereas that for calc-alkaline affinity is 200 MPa. Rhyolitic melts (SiO_2 >72 wt %) having calc-alkaline or tholeiitic affinities require shallow conditions to be generated (100–200 MPa; Fig. 11a).

It should be noted that, apart from the difference in temperature, pressure and oxygen fugacity, volatile exsolution during magma ascent could also control or enhance the tholeiitic or calc-alkaline affinity of the magma, in particular if the magma stored at deep level is water rich and moderately reduced. As an example, our results indicate that, at Santorini, the deep tholeiitic dacitic–rhyodacitic liquids generated at 400 MPa at NNO + 0·5 could contain up to 7–8 wt % H_2O_{melt} (Tables 2 and 9). The decompression of such volatile-rich melts will inevitably promote fluid exsolution at around 300 MPa, which could increase the prevailing fO_2, as shown by numerical simulations for felsic melts (Burgisser *et al.*, 2008). The increase in oxidation state of the system via such a process will depend on the final pressure reached. At 100 MPa almost half of the amount of H_2O_{melt} is expelled out of the magma and the corresponding increase in fO_2 will be stronger than in the magma stored at 200 MPa, if H_2O exsolution drives oxidation (but also see Waters & Lange, 2016). We note, however, that decompression may also lead to reduction of magmas (e.g. Gaillard & Scaillet, 2014; Moussallam *et al.*, 2014), so there is no unique answer to the effect of degassing on fO_2.

Apart from volatile exsolution effects, which could either counteract or amplify apparent redox effects on the LLD, our experimental data indicate that the FeO*/MgO of magmas can be used to a first approximation as a proxy to estimate their ponding level or melt generation conditions, as we illustrate below for several Santorini eruptions.

The plumbing system of single major and minor eruptions at Santorini

Recent eruptions from Santorini are characterized by intermediate (andesite to dacite) to silicic magmas (evolved dacites to rhyodacites) that volumetrically dominate the sequence. However, when the FeO*/MgO ratio of such magmas is considered, it is possible to observe that each eruption generally tapped liquids having mostly either tholeiitic (i.e. Vourvolous, Lower Pumice 1), or calc-alkaline (Minoan) or a mix of both affinities (i.e. Lower Pumice 2, Cape Riva (Fig. 11*a*; Druitt *et al.*, 1999). In what follows, we combine the different FeO*/MgO ratios of the erupted magmas with our experimental results and previous geochemical and thermal constraints from the literature to provide insights on the possible origin and/or source levels of the magmas involved during single eruptions of Santorini. We stress again that such an approach must be considered as a first approximation to depth assessment, with a precision of ±40 MPa.

Minoan

Minoan andesites, dacites and the majority of the rhyodacitic products have calc-alkaline affinities with just a small part of the rhyodacites and some hornblende-bearing dioritic nodules having FeO*/MgO ratios that fall into the tholeiitic field (Fig. 11a; Cottrell *et al.*, 1999; Druitt *et al.*, 1999; Druitt, 2014). Pre-eruption temperatures for rhyodacitic products are ≤900 °C (Cottrell *et al.*, 1999; Druitt *et al.*, 1999; Cadoux *et al.*, 2014; Druitt, 2014) whereas temperatures of 990–1016°C were inferred by Michaud *et al.* (2000) for the andesitic enclaves dispersed within the more evolved products. Accordingly, the majority of the andesite to rhyodacite calc-alkaline products plot in the 200 MPa field

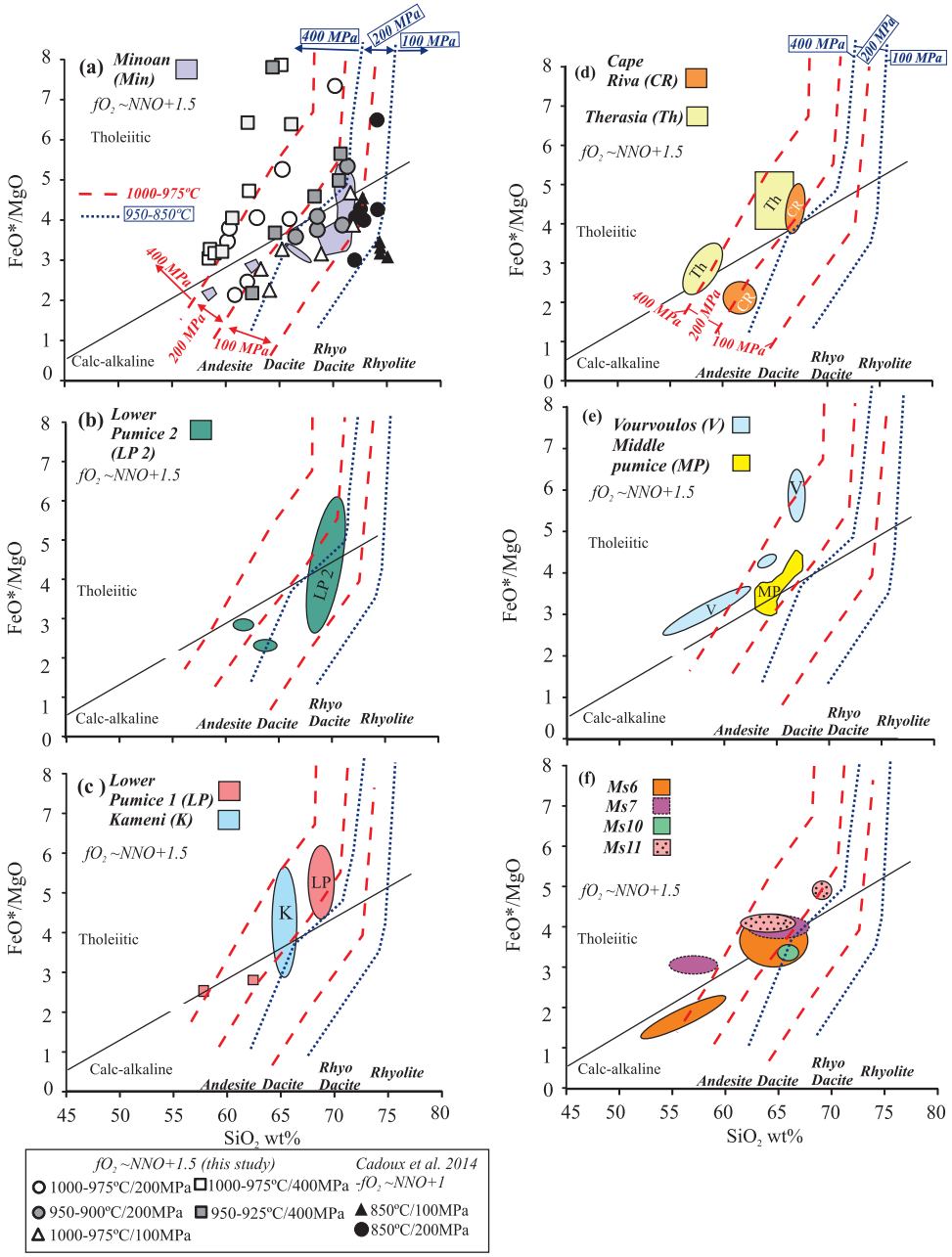

Fig. 11. FeO*/MgO vs SiO_2 and tholeiitic and calc-alkaline affinities of (a–e) Santorini recent major (silicic- and intermediate-dominated compositions) and (f) interplinian eruptions. Natural rock data from Barton & Huijsmans (1986), Gardner *et al.* (1996), Cottrell *et al.* (1999), Druitt *et al.* (1999), Vespa *et al.* (2006), Gertisser *et al.* (2009), Fabbro *et al.* (2013) and Druitt (2014). Errors are equal to symbol size. Red dashed lines and blue dotted lines are explained in the text.

(Fig. 11a). However, the occurrence of a minor group of tholeiitic rhyodacites and hornblende dioritic nodules does suggest that liquids coming from deeper levels (400 MPa) were also involved in the eruption (Cottrell *et al.*, 1999; Druitt *et al.*, 1999; Druitt, 2014). These results are altogether consistent with previous depth estimates for Minoan products (Cottrell *et al.*, 1999; Cadoux *et al.*, 2014), andesites at Santorini (this work), and venting models proposed by Druitt (2014) for this eruption: the main calc-alkaline reservoir was lying at levels of 7–8 km (200 MPa; Cottrell *et al.*, 1999; Cadoux *et al.*, 2014; this work), built by multiple injections of deep-sourced (12–15 km), hot, silicic magma, which, following our results, could be represented by the small tholeiitic rhyodacitic group (Fig. 11a). Andesites occur as disseminated blobs in the Minoan products. Such blobs arise either from late-stage injection of hot andesitic magma into the main reservoir or, instead, via the remobilization of a pre-existing Ba-rich andesite intrusion during the build-up of the reservoir (Druitt, 2014). In either case, both compositions were erupted together during the first phase of the eruption (Druitt, 2014),

which necessarily indicates that both compositions were stored at the same depth (200 MPa) before the eruption.

Lower Pumice 2 and 1

Lower Pumice 2 (LP2) products have an FeO*/MgO distribution that is similar to the Minoan one but with a tholeiitic rhyodacitic group that extends towards higher ratios (Fig. 11b). Because temperatures for the mafic magmas and more evolved compositions are 1025°C and <900°C (Gertisser *et al.*, 2009; Cadoux *et al.*, 2014), again similar to those of the Minoan, this indicates that LP2 magmas were stored between 200 and 400 MPa, but in this case, with a higher contribution of deeper liquids (Fig. 11b). The distribution of LP2 and Minoan products contrasts with that of Lower Pumice 1, in which all products have clear tholeiitic affinities, indicating that, in this case, liquids erupted mostly from a 400 MPa level according to the low temperatures estimated for LP1 rhyodacitic magmas (<900°C, Cadoux *et al.*, 2014; Fig. 11c).

Therasia and Cape Riva

The Therasia and Cape Riva (CR) eruptions are separated in time by only 3000 years, and erupted similar dacitic magmas (879 ± 15°C; Fabbro *et al.*, 2013; Cadoux *et al.*, 2014). Dacitic emissions were accompanied in both cases by the co-eruption of an andesite, which, according to Fabbro *et al.* (2013), is the product of the mixing between the dacite and a basaltic magma. This is suggested by textural and chemical features of the eruptive products (i.e. presence of sawtooth plagioclase zoning, lower FeO* melt contents compared with their fractionated counterparts of Santorini; Fig. 1). However, despite their apparent similarities, the Therasia and Cape Riva products differ in their incompatible elements (i.e. K, Zr) and rare earth elements (REE), which rules out any genetic relationship between the magmas (Fabbro *et al.*, 2013). Moreover, when the FeO*/MgO melt ratios of both eruptions are considered, the products also differ (Fig. 11d); dacitic and andesitic products of Therasia show mainly tholeiitic affinities, whereas in the case of Cape Riva, two-thirds of the products have a dominantly calc-alkaline character. Considering the temperatures estimated for the dacitic (880°C; Fabbro *et al.*, 2013) and andesitic magmas (1000°C; this work) and the distribution of erupted products in Fig. 11d, a pressure of 400 MPa can be inferred for the whole Therasia magma series. In contrast, the fact that Cape Riva products straddle the tholeiitic–calc-alkaline boundary line suggests that contributions from two different levels (pressures) occurred prior to the eruption: 200 MPa for calc-alkaline andesites and 400 MPa for the tholeiitic dacites. In this case, the 200 MPa estimate can be extended towards shallower levels as the Cape Riva andesite group straddles the 200–100 MPa fields (Fig. 11d), suggesting that this was probably the depth of mixing and hybrid generation prior to the Cape Riva eruption. In the case of Cape Riva our estimates encompass the pressure constraints of 200 MPa obtained by Cadoux *et al.* (2014) based on phase equilibrium experiments.

Middle Pumice and Vourvoulous

We have applied the same reasoning to these dominantly intermediate-type eruptions. Middle Pumice juvenile products are dominated by a dacitic component and a minor evolved andesite, separated by a small compositional gap (Druitt *et al.*, 1999). Previous temperature estimates for the Middle Pumice dacites are about 890°C (Gardner *et al.*, 1996) whereas $T > 1000$°C can be assumed for the more andesitic magma (Michaud *et al.*, 2000; this work). Considering these temperatures, pressures between 400 and 200 MPa can be inferred for the dacitic and andesitic products. The small compositional gap and the presence of reverse compositional zoning in the phenocrysts (Druitt *et al.*, 1999) suggest that a short-duration mixing episode took place at levels pressures as low as 200 MPa. There are no temperature estimates for Vourvoulos magmas yet; however, in view of their petrological and chemical similarities (i.e. presence of ilmenite; Druitt *et al.*, 1999) to other Santorini magmas (Druitt *et al.*, 1999), similar temperature conditions for the Vourvoulos magmas can be inferred (<900°C for dacites, 1000°C for andesites), which yield pressures of about 400 MPa for the two compositions (Fig. 11e).

Interplinian pyroclastic deposits

Between major Plinian eruptions, smaller eruptive events (known as interplinian pyroclastic eruptions, Ms 6 to 11; Fig. 11f) also occurred, generating in this case ash, scoria and pumice (Druitt *et al.*, 1999; Vespa *et al.*, 2006). Compositionally and petrologically the interplinian eruptions are similar to major plinian eruptions. The main difference is that mafic compositions predominate in the interplinian volcanic record (Fig. 11f; Druitt *et al.*, 1999; Vespa *et al.*, 2006). The FeO*/MgO ratios of these eruptions spread over the 200 and 400 MPa fields: however, these estimates could be expanded towards shallower conditions (100 MPa) if ilmenite is part of the phenocryst assemblage. According to our results the presence of this phase constrains temperature to >975°C, which, along with the FeO*/MgO ratio of the melts (<2·5) and their SiO_2 contents (<65 wt %), point to pressures as low as 100 MPa for the reservoir.

Kameni

The post-caldera Kameni products are characterized by a homogeneous dacitic composition, as described by Barton & Huijsmans (1986). Those researchers constrained pre-eruptive temperatures at 960–1012°C based on pyroxene thermometry. Ilm was not found in any of the studied samples, in agreement with our results concerning the temperature dependence of Ilm crystallization in Santorini magmas. The distribution of

FeO*/MgO for Kameni products combined with available temperature estimates constrain pressures to between 100 and 200 MPa for the Kameni dacites (Fig. 11c). This is in general agreement with the estimates of Barton & Huijsmans (1986), who used the Cpx–Pl geobarometer to constrain pressures between 80 and 150 MPa for Kameni dacites. These results point towards shallow ponding conditions for the Kameni magmas (3–6 km), at depths that are similar to those calculated for the recent unrest episode in 2011–2012 (~4 km; Newman *et al.*, 2012; Parks *et al.*, 2012; Foumelis *et al.*, 2013; Papoutsis *et al.*, 2013).

However, the recent study of Druitt (2014) on the products of the AD 726 eruption found ilmenite and constrained pre-eruptive temperatures by using Fe–Ti oxythermometers to be between 900 and 930°C. This lower temperature increases pressure estimates to higher values (400 MPa) for the AD 726 event (Fig. 11). Altogether the Barton & Huijsmans (1986) and Druitt (2014) data are consistent with the hypothesis proposed by Martin *et al.* (2008) and Parks *et al.* (2012) in which Kameni magmas could evolve at high pressures (400 MPa) and then be injected upwards to 100–200 MPa for a short period of time (Martin *et al.*, 2008).

We conclude that intermediate eruptions of tholeiitic affinity probably tapped andesite and dacite magma reservoirs located at depths equivalent to pressures of 200 MPa and temperatures of 1000–975°C (i.e. USC-1 and USC-2 eruptions). In contrast, silicic-dominated (dacite–rhyodacite) eruptions could originate from somewhat cooler (950–900°C) and deeper reservoirs (400 MPa) if tholeiitic, or from shallower ones (200 to 100 MPa) if calc-alkaline. These results reinforce previous observations concerning the complexity of the plumbing system at Santorini volcano (Martin *et al.*, 2008; Druitt *et al.*, 2012; Fabbro *et al.*, 2013; Druitt, 2014) and can be used to understand the different compositional signatures of magmas involved during single eruptions at Santorini.

We stress here that the intensive conditions (T, P, fO_2) inferred for dacitic to rhyodacitic eruptions mostly reflect those of melt generation occurring from a USC-1 type andesite by crystal fractionation processes. In fact, our estimates largely overlap with previous storage constraints inferred for these eruptions (i.e. Minoan; Lower Pumice 2; Cape Riva; see above) so the liquid composition, in some instances, does also mimic those of equilibration prior to eruption. Nevertheless, we are aware of the limitations of our working procedure: in some cases liquids can record deeper source conditions that could be different from those registered by magmas, phenocrysts or melt inclusions (e.g. Lower Pumice 1; Cadoux *et al.*, 2014; this work). In contrast, phenocrysts or melt inclusions could potentially record shallower conditions or short periods of storage than those of liquids (e.g. Kameni; interplinian eruptions; Druitt *et al.*, 2016).

CONCLUSIONS

The structure of the recent Thera plumbing system

The combination of information concerning the melt generation and storage conditions of different eruptions over the historical record allows us to reconstruct the structure and temporal evolution of the volcanic plumbing system.

Following Andújar *et al.* (2015), Santorini basalts migrating from the mantle stagnate at depths of 12–15 km from where they can either erupt directly (Fig. 12, arrow 1) or fractionate to generate andesitic liquids. These can in turn move towards shallower levels (6–8 km, 200 MPa), pond and create reservoirs feeding major intermediate eruptions such as USC-1 and USC-2 (Fig. 12, arrow 2; this work). The subsequent fractionation of these shallow andesites yields calc-alkaline dacite and rhyodacite derivatives such as those of the Minoan and Lower Pumice 2 eruptions (Figs 10 and 11; Fig. 12, arrows 3). In contrast, when the andesites generated at a depth of 12–15 km keep fractionating there, the process produces dacitic to rhyodacitic liquids of tholeiitic affinity, similar to those feeding Lower Pumice 1, Therasia and Ms11 interplinian eruptions (Figs 10 and 11; Fig. 12, arrows 4). However, during the ascent from depth towards the surface, these evolved tholeiitic liquids can intercept shallow calc-alkaline andesitic to rhyodacitic reservoirs, as suggested previously for the Lower Pumice 2, Cape Riva and Minoan eruptions (Fig. 12, arrow 5). The difference in depth between major eruptions separated by a short time interval could thus explain why eruptions having similar mineral assemblages, compositions and volumes may or may not generate calderas (i.e. Lower Pumice 1 and 2; Cape Riva and Therasia eruptions). This suggests a plumbing system in which magmatic reservoirs at different structural levels can coexist in time (Fabbro *et al.*, 2013).

The fact that melts from different depths were involved in single eruptions could explain the presence of rare amphibole in recent pyroclastic products (Minoan; Lower Pumice 2; Cottrell *et al.*, 1999; Gertisser *et al.*, 2009), as, according to our results, the generation of dacitic–rhyodacitic melts requires $T < 925$°C and amphibole fractionation (Fig. 3). This would explain in turn the variability observed in H_2O_{melt} contents in melt inclusions from Minoan products (Druitt *et al.*, 2016) and the complex zonation patterns recorded in plagioclase phenocrysts from this eruption (Druitt *et al.*, 2012). Melt extraction from different depths prior to or during caldera-forming eruptions is not an uncommon process in large silicic eruptions (e.g. Bishop Tuff; Wallace *et al.*, 1995).

The presence of basaltic andesites carrying a mafic fingerprint (i.e. USC-1) or the occurrence of basaltic enclaves dispersed within the more felsic products indicates that mafic magmas generated at 12–15 km can intercept the shallower silicic reservoirs and trigger the eruption, mix and generate hybrid magmas such as

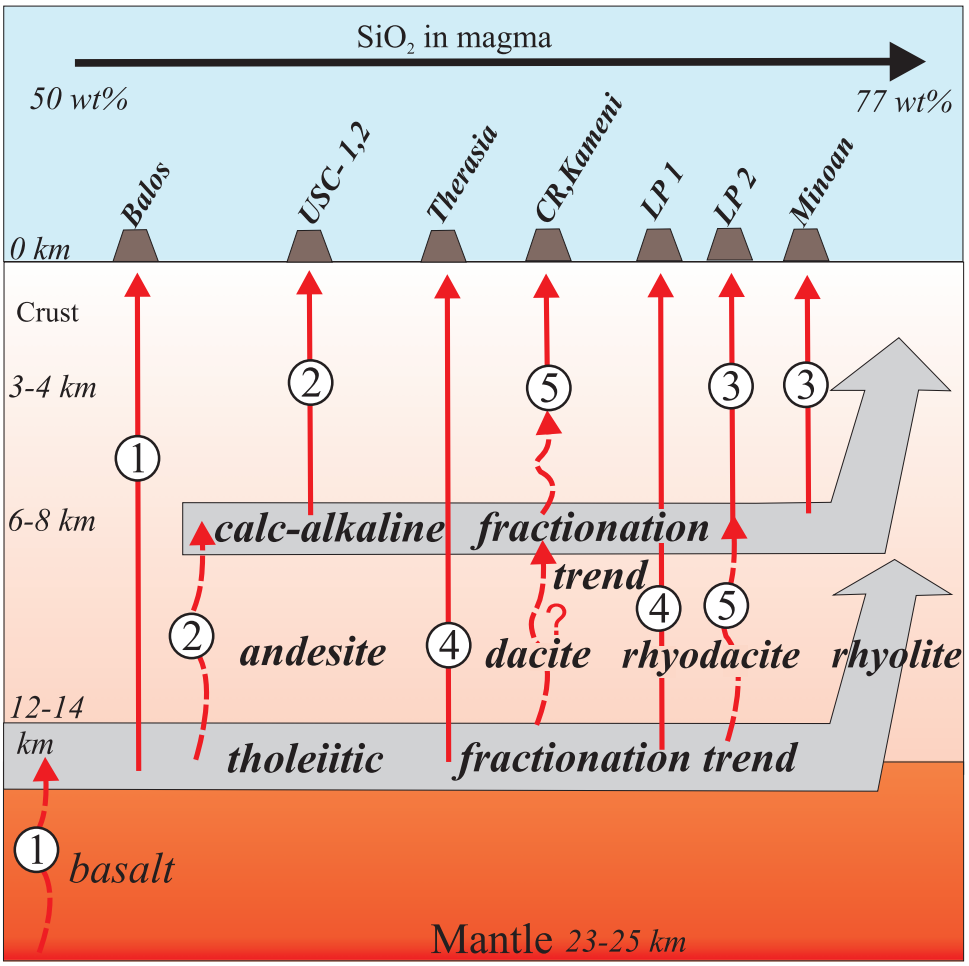

Fig. 12. Schematic view of the plumbing system of the recent Therassia volcanism (see text for details). Eruptions: USC-1,-2, Upper Scoriae 1 and 2; CR, Cape Riva; LP1 and LP2, Lower Pumice 1 and 2. Continuous-line arrows indicate direct magma supply and eruption (1–4). Dashed-line arrows show magma ascent, storage and fractionation (1, 2) and/or interaction with shallower reservoirs (5).

Therasia–Cape Riva or, instead, pass through the shallow reservoirs and produce mafic eruptions (Fabbro *et al.*, 2013; Andújar *et al.*, 2015).

The depths inferred for the recent Kameni magmas (4–6 km) are slightly shallower than those inferred for most of the major silicic eruptions (i.e. 7–8 km for Minoan and Lower Pumice 2 magmas). The fact that recent magmas could be stored at shallower levels (4 km) after a caldera-forming process suggests that, following each collapse, the volcanic edifice is mostly destroyed and major restructuring of the plumbing system takes place, as suggested, for instance, for Vesuvius (Scaillet *et al.*, 2008) or Mt St Helens (Gardner *et al.*, 1996). Magmas can then reach shallow depths during the first stages of the reactivation of the volcano. However, the subsequent surface accumulation of erupted material builds a new edifice, leading to an increase of the vertical compressive stress field, which would prevent silicic magmas from reaching shallow depths, forcing them to pond at increasing pressures as the edifice grows (Pinel & Jaupart, 2000; Scaillet *et al.*, 2008).

ACKNOWLEDGEMENTS

J.A., B.S. and M.P. thank Dr I. Di Carlo for technical support with SEM–electron microprobe analysis. We thank Duncan Muir, Gerhard Worner and an anonymous reviewer for their insightful reviews, which improved the paper.

FUNDING

This work was partly funded by the ANR STOMIXSAN, contract no. ANR08CEAO80, by the INSITU project of région Centre, and equipex PLANEX (ANR-11-EQPX36), and LABEX VOLTAIRE. This is Laboratory of Excellence ClerVolc contribution number 136.

SUPPLEMENTARY DATA

Supplementary data for this paper are available at *Journal of Petrology* online.

REFERENCES

Almeev, R. R., Holtz, F., Ariskin, A. A. & Kimura, J.-I. (2013). Storage conditions of Bezymianny Volcano parental magmas: results of phase equilibria experiments at 100 and 700 MPa. *Contributions to Mineralogy and Petrology* **166**, 1389–1414.

Andújar, J., Scaillet, B., Pichavant, M. & Druitt, T. H. (2015). Differentiation conditions of a basaltic magma from Santorini, and its bearing on the production of andesite in arc settings. *Journal of Petrology* **56**, 765–794.

Baker, D. R. & Eggler, D. H. (1987). Compositions of anhydrous and hydrous melts coexisting with plagioclase, augite, and olivine or low-Ca pyroxene from 1 atm to 8 kbar: application to the Aleutian volcanic center of Atka. *American Mineralogist* **72**, 12–28.

Barton, M. & Huijsmans, J. P. P. (1986). Post-caldera dacites from the Santorini volcanic complex, Aegean Sea, Greece: an example of the eruption of lavas of near-constant composition over a 2200 year period. *Contributions to Mineralogy and Petrology* **94**, 472–495.

Barton, M., Salters, V. J. M. & Huijsmans, J. P. P. (1983). Sr-isotope and trace element evidence for the role of continental crust in calc-alkaline volcanism on Santorini and Milos, Aegean Sea, Greece. *Earth and Planettary Sciences Letters* **63**, 273–291.

Berndt, J., Koepke, J. & Holtz, F. (2005). An experimental investigation of the influence of water and oxygen fugacity on differentiation of MORB at 200 MPa. *Journal of Petrology* **46**, 135–167.

Bond, A. & Sparks, R. S. J. (1976). The Minoan eruption of Santorini, Greece. *Journal of the Geological Society, London* **132**, 1–16.

Burgisser, A. & Scaillet, B. (2007). Redox evolution of a degassing magma rising to the surface. *Nature* **445**, 194–197.

Burgisser, A., Scaillet, B. & Vardhan, H. (2008). Chemical patterns of erupting silicic magmas and their influence on the amount of degassing during ascent. *Journal of Geophysical Research* **113**, B12204.

Cadoux, A., Scaillet, B., Druitt, T. H. & Deloule, E. (2014). Magma storage conditions of large Plinian eruptions of Santorini. *Journal of Petrology* **55**, 1129–1171.

Castro, A., Vogt, K. & Gerya, T. (2013). Generation of new continental crust by sublithospheric silicic-magma relamination in arcs: A test of Taylor's andesite model. *Gondwana Research* **23**, 1554–1566.

Chou, I.-M. (1978). Calibration of oxygen buffers at elevated *P* and *T* using the hydrogen fugacity sensor. *American Mineralogist* **63**, 690–703.

Cottrell, E., Gardner, J. E. & Rutherford, M. J. (1999). Petrologic and experimental evidence for the movement and heating of the pre-eruptive Minoan rhyodacite (Santorini, Greece). *Contributions to Mineralogy and Petrology* **135**, 315–331.

Deer, W. A., Howie, R. A. & Zussman, J. (1972). *Rock-forming Minerals, Vol. 4: Framework Silicates*. Longman, 435 pp.

Devine, J. D., Gardner, J. E., Brack, H. P., Layne, G. D. & Rutherford, M. J. (1995). Comparison of microanalytical methods for estimating H_2O contents of silicic volcanic glasses. *American Mineralogist* **80**, 319–328.

Di Carlo, I., Pichavant, M., Rotolo, S. G. & Scaillet, B. (2006). Experimental crystallization of a high-K arc basalt: the golden pumice, Stromboli volcano (Italy). *Journal of Petrology* **47**, 1317–1343.

Druitt, T. H. (2014). New insights into the initiation and venting of the Bronze-Age eruption of Santorini (Greece), from component analysis. *Bulletin of Volcanology* **76**, 794.

Druitt, T. H., Mellors, R. M., Pyle, D. M. & Sparks, R. S. J. (1989). Explosive volcanism on Santorini, Greece. *Geology Magazine* **126**, 95–126.

Druitt, T. H., Edwards, L., Mellors, R. M., Pyle, D. M., Sparks, R. S. J., Lanphere, M., Davies, M. & Barriero, B. (1999). *Santorini Volcano. Geological Society, London, Memoirs* **19**, 165 pp.

Druitt, T. H., Costa, F., Deloule, E., Dungan, M. & Scaillet, B. (2012). Decadal to monthly timescales of magma transfer and reservoir growth at a caldera volcano. *Nature* **482**, 7780.

Druitt, T. H., Mercier, M., Deloule, E., Florentin, L., Cluzel, N., Médard, E. & Cadoux, A. (2016). Magma storage and extraction associated with plinian and interplinian activity at Santorini caldera (Greece). *Journal of Petrology* **57**, 461–494

Eichelberger, J. C. (1978). Andesitic volcanism and crustal evolution. *Nature* **275**, 21–27.

Fabbro, G. N., Druitt, T. H. & Scaillet, S. (2013). Evolution of the crustal magma plumbing system during the build-up to the 22-ka caldera-forming eruption of Santorini. *Bulletin of Volcanology* **75**, 767.

Foumelis, M., Trasatti, E., Papageorgiou, E., Stramondo, S. & Parcharidis, I. (2013). Monitoring Santorini volcano (Greece) breathing from space. *Geophysical Journal International* **193**, 161–170.

Gaillard, F. & Scaillet, B. (2014). A theoretical framework for volcanic degassing chemistry in a comparative planetology perspective and implications for planetary atmospheres. *Earth and Planetary Science Letters* **403**, 307–316.

Gardner, J. E., Thomas, R. M. E., Jaupart, C. & Tait, S. (1996). Fragmentation of magma during Plinian volcanic eruptions. *Bulletin of Volcanology* **58**, 144–162.

Gertisser, R., Preece, K. & Keller, J. (2009). The Plinian Lower Pumice 2 eruption, Santorini, Greece: Magma evolution and volatile behaviour. *Journal of Volcanology and Geothermal Research* **186**, 387–406.

Gill, J. B. (1981). *Orogenic Andesites and Plate Tectonics*. Springer, 390 pp.

Green, T. H. & Ringwood, A. E. (1968). Genesis of the calc-alkaline igneous rock suite. *Contributions to Mineralogy and Petrology* **18**, 105–162.

Grove, T. L., Baker, M. B., Price, R. C., Parman, S. W., Elkins-Tanton, L. T., Chatterjee, N. & Müntener, O. (2005). Magnesian andesite and dacite lavas from Mt. Shasta, northern California: products of fractional crystallization of H_2O-rich mantle melts. *Contributions to Mineralogy and Petrology* **148**, 542–565.

Heiken, G. & McCoy, F., Jr (1984). Caldera development during the Minoan eruption, Thira, Cyclades, Greece. *Journal of Geophysical Research* **89**, 8441–8462.

Huijsmans, J. P. P. & Barton, M. (1989). Polybaric geochemical evolution of two shield volcanoes from Santorini, Aegean Sea, Greece: evidence for zoned magma chambers from cyclic compositional variations. *Journal of Petrology* **30**, 583–625.

Huijsmans, J. P. P., Barton, M. & Salters, V. J. M. (1988). Geochemistry and evolution of the calc-alkaline volcanic complex of Santorini, Aegean Sea, Greece. *Journal of Volcanology and Geothermal Research* **34**: 283–306.

Iacono-Marziano, G., Gaillard, F. & Pichavant, M. (2008). Limestone assimilation by basaltic magmas: an experimental re-assessment and application to Italian volcanoes. *Contributions to Mineralogy and Petrology* **155**, 719–738.

Karagianni, E. E. & Papazachos, B. C. (2007). Shear velocity structure in the Aegean area obtained by joint inversion of Rayleigh and Love waves. In: Taymaz, T., Yilmaz, Y. & Dilek, Y. (eds) *The Geodynamics of the Aegean and Anatolia.*

Geological Society, London, Special Publications **291**, 159–181.

Keller, J., Kraml, M. & Schwarz, M. (2000). Dating major volcanic paroxysms within the deep-sea record: the example of the Thera Formation, Santorini, Greece. In: *Exploring volcanoes: utilization of their resources and mitigation of their hazards: abstracts addresses QE521.5 I38 2000, IAVCEI General Assembly, Bali, Indonesia, July 18–22*. Volcanological Survey of Indonesia, p. 16.

Konstantinou, K. I. (2010). Crustal rheology of the Santorini–Amorgos zone: Implications for the nucleation depth and rupture extent of the 9 July 1956 Amorgos earthquake, southern Aegean. *Journal of Geodynamics* **50**, 400–409.

Laumonier, M., Scaillet, B., Pichavant, M., Champallier, R., Andújar, J. & Arbaret, L. (2014). On the conditions of magma mixing and its bearing on andesite production in the crust. *Nature Communications* **5**, 5607.

Leake, B. E., Woolley, A. R., Arps, C. E. S., et al. (1997). Nomenclature of amphiboles: report of the subcommittee on amphiboles of the International Mineralogical Association Commission on New Minerals and Mineral Names. *Mineralogical Magazine* **61**, 295–321.

Le Bas, M. J. & Streckeisen, A. L. (1991). The IUGS systematics of igneous rocks. *Journal of the Geological Society, London* **148**, 825–833.

Le Pichon, X. & Angelier, J. (1979). The Hellenic arc and trench system: A key to the neotectonic evolution of the eastern Mediterranean area. *Tectonophysics* **60**, 1–42.

Mann, A. C. (1983). Trace element geochemistry of high alumina basalt–andesite–dacite–rhyodacite lavas of the Main Volcanic Series of Santorini Volcano, Greece. *Contributions to Mineralogy and Petrology* **395**, 43–57.

Martel, C., Pichavant, M., Holtz, F. & Scaillet, B. (1999). Effects of fO_2 and H_2O on andesite phase relations between 2 and 4 kbar. *Journal of Geophysical Research* **104**, 29,453–29,470.

Martin, V., Morgan, D. J., Jerram, D. J., Caddick, M. J., Prior, D. J. & Davidson, J. P. (2008). Bang! month-scale eruption triggering at Santorini volcano. *Science* **321**, 1178.

Martin, V. M., Davidson, J., Morgan, D. & Jerram, D. A. (2010). Using the Sr 1097 isotope compositions of feldspars and glass to distinguish magma 1098 system components and dynamics. *Geology* **38**, 539–542.

Mellors, R. A. & Sparks, R. S. J. (1991). Spatter-rich pyroclastic flow deposits on Santorini, Greece. *Bulletin of Volcanology* **53**, 327–342.

Michaud, V., Clocchiatti, R. & Sbrana, S. (2000). The Minoan and post-Minoan eruptions, Santorini (Greece), in the light of melt inclusions: chlorine and sulphur behaviour. *Journal of Volcanology and Geothermal Research* **99**, 195–214.

Miyashiro, A. (1974). Volcanic rock series in island arcs and active continental margins. *American Journal of Science* **274**, 321–355.

Morimoto, N. (1989). Nomenclature of pyroxenes. Subcommittee on pyroxenes. Commission on new minerals and mineral names. *Canadian Mineralogist* **27**, 143–156.

Mortazavi, M. & Sparks, R. S. J. (2004). Origin of rhyolite and rhyodacite lavas and associated mafic inclusions of Cape Akrotiri, Santorini: the role of wet basalt in generating calc-alkaline silicic magmas. *Contributions to Mineralogy and Petrology* **146**, 397–413.

Moussallam, Y., Oppenheimer, C., Scaillet, B., Gaillard, F., Kyle, P., Peters, N., Hartley, M., Berlo, K. & Donovan, A. (2014). Tracking the changing oxidation state of Erebus magmas, from mantle to surface, driven by magma ascent and degassing. *Earth and Planetary Science Letters* **393**, 200–209.

Newman, A. V., Stiros, S., Feng, L., Psimoulis, P., Moschas, F., Saltogianni, V., Jiang, Y., Papazachos, C., Panagiotopoulos, D., Karagianni, E. & Vamvakaris, D. (2012). Recent geodetic unrest at Santorini Caldera, Greece. *Geophysical Research Letters* **39**, L06309.

Nichols, I. A. (1971a). Petrology of Santorini volcano, Cyclades, Greece. *Journal of Petrology* **12**, 67–119.

Nichols, I. A. (1971b). Calcareous inclusions in lavas and agglomerates of Santorini volcano. *Contributions to Mineralogy and Petrology* **30**, 261–276.

Nocquet, J.-M. (2012). Present-day kinematics of the Mediterranean: a comprehensive overview of GPS results. *Tectonophysics* **579**, 220–242.

Papale, P., Moretti, R. & Barbato, D. (2006). The compositional dependence of the saturation surface of $H_2O + CO_2$ fluids in silicate melts. *Chemical Geology* **229**, 78–95.

Papazachos, B. C., Karakostas, V. G., Papazachos, C. B. & Scordilis, E. M. (2000). The geometry of the Wadati–Benioff zone and lithospheric kinematics in the Hellenic arc. *Tectonophysics* **319**, 275–300.

Papoutsis, I., Papanikolaou, X., Floyd, M., Ji, K. H., Kontoes, C., Paradissis, D. & Zacharis, V. (2013). Mapping inflation at Santorini volcano, Greece, using GPS and InSAR. *Geophysical Research Letters* **40**, 267–272.

Parks, M. M., Biggs, J., England, P., Mather, T. A., Nomikou, P., Palamartchouk, K., Papanikolaou, X., Paradissis, D., Parsons, B., Pyle, D. M., Raptakis, C. & Zacharis, V. (2012). Evolution of Santorini Volcano dominated by episodic and rapid fluxes of melt from depth. *Nature Geoscience* **5**, 749–754.

Pichavant, M., Martel, C., Bourdier, J.-L. & Scaillet, B. (2002). Physical conditions, structure and dynamics of a zoned magma chamber: Mt. Pelée (Martinique, Lesser Antilles arc). *Journal of Geophysical Research* **107**, doi:10.1029/2001JB000315.

Pinel, V. & Jaupart, C. (2000). The effect of edifice load on magma ascent beneath a volcano, *Philosophical Transactions of the Royal Society of London* **358**, 1515–1532.

Pownceby, M. I. & O'Neill, H. St. C. (1994). Thermodynamic data from redox reactions at high temperatures. III. Activity–composition relations in Ni–Pd alloys from EMF measurements at 850–1250 K and calibration of the NiO + Ni–Pd assemblage as a redox sensor. *Contributions to Mineralogy and Petrology* **116**, 327–339.

Pyle, D. M. & Elliott, J. R. (2006). Quantitative morphology, recent evolution, and future activity of the Kameni Islands volcano, Santorini, Greece. *Geosphere* **2**, 253–268.

Ruprecht, P., Bergantz, G. W., Cooper, K. M. & Hildreth, W. (2012). The crustal magma storage system of Volcán Quizapu, Chile, and the effects of magma mixing on magma diversity. *Journal of Petrology* **53**, 801–840.

Scaillet, B., Pichavant, M. & Cioni, R. (2008). Upward migration of Vesuvius magma chamber over the past 20,000 years. *Nature* **455**, 216–219.

Scaillet, B. & Macdonald, R. (2006). Experimental and thermodynamic constraints on the sulphur yield of peralkaline and metaluminous silicic flood eruptions. *Journal of Petrology* **47**, 1413–1437.

Scaillet, B. & Evans, B. W. (1999). The 15 June 1991 eruption of Mount Pinatubo. I. phase equilibria and Pre-eruption P-TfO_2-aH_2O. *Journal of Petrology* **40**, 381–411.

Sisson, T. W. & Grove, T. L. (1993). Experimental investigations of the role of H_2O in calc-alkaline differentiation and subduction zone magmatism. *Contributions to Mineralogy and Petrology* **113**, 143–166.

Spandler, C., Martin, L. H. J. & Pettke, T. (2012). Carbonate assimilation during magma evolution at Nisyros (Greece), South Aegean Arc: Evidence from clinopyroxenite xenoliths. *Lithos* **146–147**, 18–33.

Tirel, C., Gueydan, F., Tiberi, C. & Brun, J.-P. (2004). Aegean crustal thickness inferred from gravity inversion. Geodynamical implications. *Earth and Planetary Science Letters* **228**, 267–280.

Vespa, M., Keller, J. & Gertisser, R. (2006). Interplinian explosive activity of Santorini volcano (Greece) during the past 150,000 years. *Journal of Volcanology and Geothermal Research* **153**, 262–286.

Wallace, P. J., Anderson, A. T. & Davis, A. M. (1995). Quantification of pre-eruptive exsolved gas contents in silicic magmas. *Nature* **377**, 612–616.

Waters, L. E. & Lange, R. A. (2016). No effect of H_2O degassing on the oxidation state of magmatic liquids. *Earth and Planetary Science Letters* **447**, 48–59.

Zellmer, G., Turner, S. & Hawkesworth, C. (2000). Timescales of destructive plate margin magmatism: new insights from Santorini, Aegean volcanic arc. *Earth and Planetary Science Letters* **174**, 265–281.